



Vein-type gold formation during late extensional collapse of the Eastern Desert, Egypt: the Gidami deposit

Basem Zoheir^{1,2} · Ryan McAleer³ · Matthew Steele-MacInnis⁴ · Armin Zeh⁵ · Wyatt Bain⁴ · Spencer Poulette⁴

Received: 26 January 2022 / Accepted: 2 November 2022
© The Author(s) 2022

Abstract

Orogenic gold deposits, though construed to focused fluid flow during orogenesis, commonly post-date the main accretionary events. Several lines of evidence indicate that orogenic gold formation in the Arabian–Nubian Shield continued through the orogen collapse stage and associated rapid exhumation and thermal re-equilibration. The Gidami gold deposit in the Eastern Desert of Egypt is associated with post-foliation, brittle-ductile shear zones that deformed a weakly foliated tonalite-trondhjemite massif dated as ~704 Ma (U–Pb zircon age). Gold-sulfide quartz veins exhibit textural features indicative of repeated mylonitization, recrystallization, and muscovite crystallization. New ⁴⁰Ar/³⁹Ar ages of muscovite flakes from the auriferous quartz veins and from the altered wallrock overlap within analytical uncertainty at ~583 Ma, which corresponds to the climax of extension-related wrenching and rapid exhumation in the region (~596 to 582 Ma). Laser ablation-inductively coupled plasma-mass spectrometry (LA-ICP-MS) data coupled with microtextural characteristics suggest that early formed pyrite generations experienced substantial fluid-mediated recrystallization, and that a set of metals was remobilized by later fluids. A late generation of fibrous pyrite, ubiquitous in microfractures, deposited while the veins re-opened and deformed. The occurrence of free gold particles along with a late-paragenetic assemblage of galena-sphalerite-chalcopyrite(± hes-site ± cervelleite) was related to influx of low salinity, metalliferous H₂O–NaCl–CO₂–CH₄ fluids as indicated by the fluid inclusion laser Raman spectroscopy and microthermometry results. Au-mobilization and redeposition at $T \leq 350$ °C and $P \sim 1$ to 1.7 kbar, triggered by intermittent fluid pluses and thermal re-equilibration, were most likely stimulated by extensional structures and within-plate magmatism. Coincident province- and deposit-scale pressure–temperature–time data highlight the pivotal role of the orogenic collapse tectonics in gold endowment in the Central Eastern Desert’s crust.

Keywords Gidami gold deposit · Eastern Desert of Egypt · Orogenic collapse structures · Fluid inclusions · Geochronological and thermochronological studies

Editorial handling: H. E. Frimmel

✉ Basem Zoheir
basem.zoheir@gmail.com; basem.zoheir@fsc.bu.edu.eg

¹ Department of Geology, Faculty of Science, Benha University, Benha 13518, Egypt

² Institute of Geosciences, University of Kiel, Ludewig-Meyn-Strasse 10, 24118 Kiel, Germany

³ United States Geological Survey, 12201 Sunrise Valley Dr, Reston, VA 20192, USA

⁴ University of Alberta, 1-26 Earth Sciences Building, Edmonton, AB T6G 2E3, Canada

⁵ Institut für Angewandte Geowissenschaften – Mineralogie und Petrologie, Karlsruher Institut Für Technologie (KIT), Adenauerring 20B, 76131 Karlsruhe, Germany

Introduction

Orogenic gold deposits comprise hydrothermal vein-type mineralization, classically interpreted to develop during late-stage, extensional shearing in accretionary orogenic belts (e.g., Kerrich and Cassidy 1994; Bierlein and Crowe 2000; Goldfarb et al. 2001; Bouchot and Moritz 2000; Groves et al. 1998, 2003). Gold-quartz vein formation is generally considered to be syn-kinematic with at least one main penetrative deformation stage, often superimposing first order orogenic fabrics (Goldfarb and Groves 2015). Fluid inclusion studies show the involvement of CO₂–H₂O–NaCl fluids and point toward the role of boiling and fluid mixing in gold deposition (e.g., Ridley and Diamond 2000; Tomkins 2013; Zoheir et al. 2019a; Li et al. 2020). The latter is commonly attributed to pressure fluctuations in a fault zone and has

been widely interpreted to be responsible for triggering the precipitation of most of the sulfides as well as gold in orogenic belts (e.g., Sibson et al. 1988; Cox 1995; Mikucki 1998). However, linkages between fluid percolation, evolution, continual pressure fluctuations and metal precipitation from hydrothermal fluids are commonly challenging to pinpoint and have not yet been comprehensively assessed (e.g., Peterson and Mavrogenes 2014).

Although some orogenic gold deposits extend over vertical distances in excess of 1 km, systematic vertical mineral zonation and ore grade variation are generally lacking (e.g., Goldfarb et al. 2001; Bierlein et al. 2004). Gold- and sulfide-bearing quartz (\pm carbonate) veins in these deposits are generally thought to form at P–T conditions less than, or near, the brittle-ductile transition, typically around 1–3 kbar and 180–350 °C (e.g., Stipp et al. 2002; Behr and Platt 2011). These ranges of P and T also match well with a survey of homogenization temperatures and pressures of aqueous-carbonic fluid inclusions from orogenic gold deposits (Steele-MacInnis et al. 2020). In most instances, fluid inclusions indicate that deposition of the ore was from generally low-salinity (≤ 7 wt.% NaCl_{eq}), CO₂-rich (up to ~50 mol%), and near-neutral fluids, and occurred via various combinations of wall-rock sulfidation reactions, fluctuation in pressure, and/or reduction–oxidation reactions (e.g. Bierlein et al. 2004;

Bodnar et al. 2014; Goldfarb and Groves, 2015; Steele-MacInnis et al. 2020).

The Eastern Desert of Egypt contains numerous occurrences of gold-bearing quartz veins and less common alluvial placers (Fig. 1A; Zoheir et al. 2019b). Most of these occurrences are spatially associated with wrench and extensional structures that deformed the Neoproterozoic shield rocks. The Gidami gold deposit (also known as Sirbakis; Klemm and Klemm 2013) is located in the Central Eastern Desert (CED) of Egypt, ~60 km west of the Red Sea (26° 23' 15" N, 33° 27' E; Fig. 1A). According to Klemm and Klemm (2013), the Gidami deposit was a significant historical gold producer in ancient times (the New Kingdom of Egypt), and was re-evaluated and operated during the last century. The Gidami deposit is one of several (~18) gold occurrences in the large Abu Marawat concession area in the CED (Fig. 1B). The concession area, 100% owned by a Canadian exploration company "Aton Resources Inc.," includes massive and sub-massive Zn-Cu \pm Ag sulfide ores, and Au-Cu mineralization in quartz veins as well as banded iron formation (BIF) (Botros 2004; Zoheir et al. 2008; Zoheir and Akawy 2010; Abd El-Rahman et al. 2015; Bampton 2017; Abd El Monsef et al. 2018; Zoheir et al. 2019b).

Gold deposits of the Abu Marawat area have been interpreted as potentially representing sheared massive-sulfide

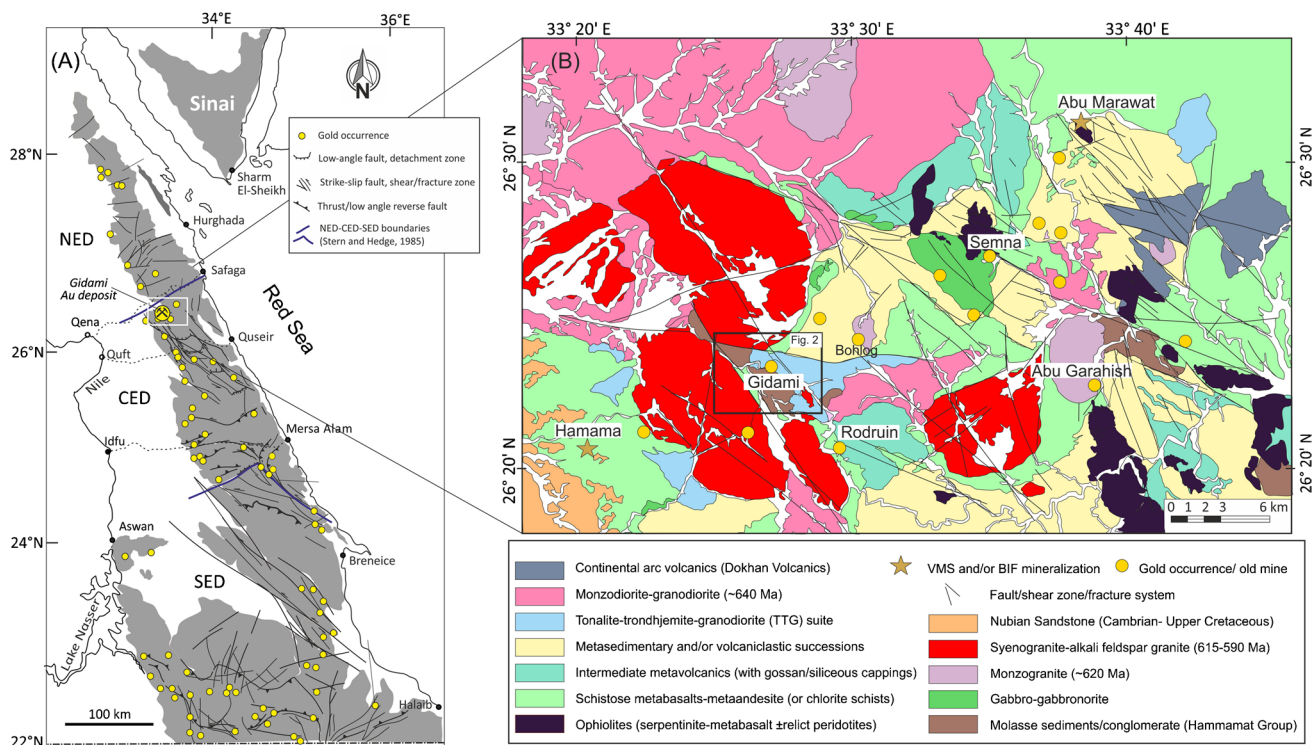


Fig. 1 (A) Distribution of gold occurrences in the Eastern Desert of Egypt. (B) Geological map of the Gidami mine area and neighboring gold, massive sulfide and banded iron formation ores (based on the

Quseir sheet Conoco Coral, 1987 compiled with new field and remote sensing work for this study)

mineralization (Valliant and Salmon 2012), but clearly share characteristics of orogenic gold (e.g., Zoheir et al. 2008; Zoheir and Akawy 2010). Hamama and Rodruin are polymetallic epithermal-VMS occurrences containing Au–Ag mineralization in oxide caps above unaltered sulfide zones (Bampton 2017; Orduña 2018). In the Abu Marawat area, two main quartz veins, subparallel less significant quartz veins, and quartz-rich gossans were tested over 800 m strike length and 20 to 250 m depth. The inferred resource of the deposit based on 98 diamond drill holes (19,573 m) is 2.9 Mt at 1.75 g/t Au, 29.3 g/t Ag, 0.77% Cu, and 1.15% Zn (Bampton 2017).

In view of the current revival of exploration and reassessment of the ancient Egyptian gold deposits, comprehensive metallogenetic studies using modern analytical techniques applied to historical deposits are needed, and may have implications for ongoing and future exploration. The Gidami deposit is one of these historical gold deposits that are spatially associated with post-orogenic extensional tectonics in the CED. It thus provides an ideal test case where ore fluid chemistry and timing relationships were not obscured by metamorphism but remained intact. Mineral chemistry and microtextures of gold-associated sulfides as well as fluid inclusion characteristics of the auriferous quartz veins from the Gidami deposit are here presented. Constraints on timing of gold mineralization are based on new LA-ICP-MS U–Pb zircon ages of the host rock and $^{40}\text{Ar}/^{39}\text{Ar}$ geochronology of hydrothermal muscovite disseminated in the mineralized quartz veins. Integrated with the trace element data of Au-associated pyrites and ore fluid characteristics, the age dating results enable an improved understanding of the processes that triggered Au ore formation at the Gidami and neighboring areas.

Geologic setting

The basement complex of the Eastern Desert of Egypt is part of the mostly Neoproterozoic Arabian-Nubian Shield (ANS). In the CED, widespread island arc volcanic and volcanoclastic successions are characterized by laminae of oxide-facies banded iron formation (BIF) (e.g., Sims and James 1984 and references therein). Less abundant ophiolitic rocks form allochthonous slabs or extensive nappes, commonly in the hanging wall of gneissic core complexes or as terranes of highly tectonized ophiolitic mélange (e.g., Shackleton 1994; Stern et al. 2004; Stern 2018). A number of NW–SE shear-bound gneissic complexes are commonly interpreted as migmatite-cored structural domes exhumed in response to an oblique tectonic regime (Neumayr et al. 1996; Fritz et al. 1996, 2002; Loizenbauer et al. 2001). These complexes thus represent the autochthonous footwall block for the allochthonous ophiolites. Oblique convergence-induced accretion of

island arcs is suggested to have resulted in sets of sub-parallel NNW-directed thrusts most likely developed between 690 and 609 Ma (Fig. 1A; Andresen et al. 2009; Augland et al. 2012). Tectonic change to left-lateral strike-slip shearing and faulting in the CED occurred at ~620–560 Ma, corresponding to the time of motion along the Najd Fault System (Stern 1985; Greiling et al. 1988).

In the study area (Figs. 1B and 2), island arc metavolcanic rocks include heterogeneously deformed dacitic and spilitized ferrobaltic flows, and pyroclastic rocks (EGSMA 1992) that are generally metamorphosed to greenschist-facies conditions. Foliated basic metavolcanic rocks prevail in the NE part of the map area whereas the central part of the area is occupied by intermediate to acidic (rhyolite, dacite, andesite) volcanic rocks. Abundant sub-aerial silicic lavas in these metavolcanic rocks suggest a mature arc setting for these rocks (e.g., Fowler et al. 2006). Coarse- and medium-grained quartz diorite and tonalite-trondhjemite-granodiorite (TTG) comprise the island arc plutonic assemblage in the area. These rocks are locally foliated and are cut by numerous basic dikes and quartz veins. Intrusions of syn-tectonic monzodiorite and granodiorite cut the island arc rocks and exhibit features of variable ductile deformation (Zoheir et al. 2021). These rocks form lowland terrains in the northern part of the study area. Fault-controlled masses of porphyritic volcanic rocks were assigned to the Dokhan volcanic rocks in the Eastern Desert (~620–590 Ma; Wilde and Youssef 2000, 2002; Eliwa et al. 2006), with geochemical characteristics suggesting formation in a setting transitional toward a stable continental craton (Ressetar and Monrad, 1983). The Dokhan volcanic rocks are associated with poorly-sorted molasse type sedimentary rocks (greywacke, siltstone and polymictic conglomerate), and are confined to NW–SE faults in the eastern part of the study area (Fig. 1B). These intramontane basin molasse sedimentary rocks are referred to as the Hammamat Group (~620–585 Ma) and rest unconformably on the basement complex of the Eastern Desert (Willis et al. 1988; Eliwa et al. 2010; Breitkreuz et al. 2010; Bezenjani et al. 2014). The Hammamat Group rocks were generally weakly metamorphosed or imprinted by local thermal aureoles next to crosscutting granitic intrusions.

Discrete intrusions of gabbro and gabbro-norite in the area cut the older metavolcanic and metavolcanoclastic rocks. South of Semna gold mine, a large exposure of gabbro-norite is also controlled by the NW–SE faults. Small intrusions of biotite monzogranite (~620 Ma, Zoheir et al. 2021) cut the foliated metavolcanic and the older granodiorite rocks and commonly form oval or subrounded surface expressions in plan view. Younger leucogranite, syenogranite, and alkali feldspar granite are undeformed and commonly associated with gamma-ray anomalies. According to Fritz et al. (1996) and Loizenbauer et al. (2001), oblique convergence and development of wrench

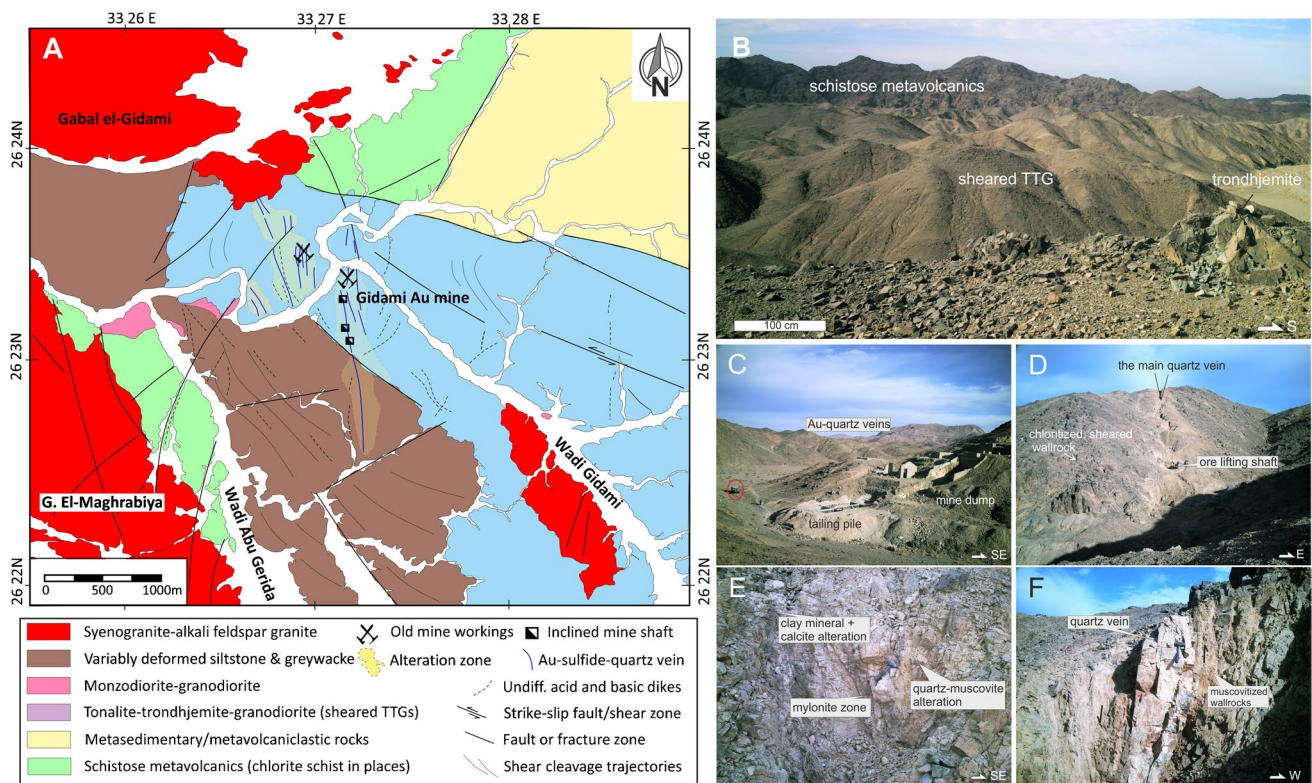


Fig. 2 (A) Geological map of the Gidami gold deposit (modified from Murr 1999). (B) NW-elongate belt of sheared tonalite-trondhjemite-granodiorite (TTG) rocks separated by a fault contact from foliated island arc metasedimentary/metavolcaniclastic rocks. (C) The early twentieth century mine plant, dump and tailing, and the northern quartz vein swarms. (D) The main quartz vein in the Gidami gold

deposit and associated altered, sheared tonalite-trondhjemite complex. (E) Different alteration types in the mylonitized host rocks close to the mineralized quartz veins. (F) Muscovite alteration bordering the mineralized quartz vein in the southern part of the mine area. Notice the pervasive muscovite and mylonitization zones bordering a sheeted quartz vein

faults resulted in NW–SE pull-apart basins and associated zones of crustal weakness likely facilitated emplacement of variably evolved granitic rocks. Sequences of the Nubian Sandstone (Cambrian–Upper Cretaceous) overlie unconformably the Precambrian basement in the southwestern part of the study area.

Several occurrences of gold mineralization are located in the area, and are hosted by different rocks but generally associated with brittle-ductile shear/fault zones. Gold only, gold-bearing VMS and BIF-hosted gold mineralization styles have been described in the province (Fig. 1B; Murr 1999; Zoheir et al. 2008; Zoheir and Akawy 2010; Abd El-Rahman et al. 2015; Bampton 2017). Mining activities for gold date back to ancient times, as early as the 2nd millennium BCE, but re-evaluation and exploitation workings were also active in the early twentieth century. Gidami is one of several gold deposits in the area that are associated with variably deformed igneous intrusions (Zoheir et al. 2015, 2018, 2019a, 2021). The mineralized quartz veins are, however, confined to mylonite zones within these intrusions, and in the case of Gidami, extend beyond the boundary of the exposed trondhjemite host rocks.

The Gidami gold deposit

The Gidami gold deposit is related to a set of ~N-S striking quartz veins in brittle-ductile shear/fault zones discordant to the main structural fabrics of the host rocks, and is accompanied by limited hydrothermal alteration haloes (Fig. 2A). In the mine area, an old processing plant is connected by a narrow and flattened trail with two open adits leading to underground stopes (Fig. 2C). A tailings pile and numerous mine buildings, probably related to mining activities at the beginning of the twentieth century, exist near the Gidami water well along the valley. Klemm and Klemm (2013) also describe some remains of ancient settlements and mining infrastructure in the area, dating back at least as early as the Ptolemaic era.

In the mine area, the main gold-bearing quartz vein extends for over 1250 m in a NNW-SSE direction, with an average width of ~1 m. This quartz vein was intensively mined from the surface to a depth of ~20 m (Fig. 2D). The workable grades were ~15 ppm Au on average (El-Ramly et al. 1970). To the northwest of the main auriferous quartz vein, swarms of smaller veins (NNW- or N-striking) have

been extensively worked by ancient miners. Most of the mineralized quartz veins cut variably deformed trondhjemite and extend southwards to cut siltstone-conglomerate of the Hamamat Group molasse sedimentary rocks. This constrains the maximum age of mineralization to ~600 Ma, because the age range of the molasse rocks is 600–580 Ma. Field observations reveal that the auriferous quartz veins cut discrete NE-SW andesitic dikes. Gold in quartz veins is associated with ubiquitous pyrite, sphalerite, chalcopyrite, and galena.

In 2017, Aton Resources Inc. assayed surface grab samples from the mineralized veins and reported high grades of ~33–150 ppm Au, and channel samples with up to 29.5 ppm Au (<https://www.atonresources.com/>). According to the company reports, surface trenching results confirmed the presence of a wide zone of gold dispersion around the narrow quartz veins. The sampling program of quartz veins in the northern extension of the main vein indicated a grade of 32.9 g/t Au from an individual grab sample, whereas trenches through the parallel vein system returned grades of 0.21 g/t Au over an interval of 109.1 m and 0.36 g/t Au over 45.85 m (Aton resources release, September 2017).

The main Au-quartz vein is associated with anastomosing thin and discontinuous veinlets and enclosing variably altered wallrocks (Fig. 2C–F). It is composed of milky quartz and contains minor disseminations of sulfides. The main vein is associated with a strongly fractured and sheared wallrock that strikes ~N-S and dips steeply easterly (Fig. 2D, F). Variations in dip, intensity of deformation, and vein style are controlled by the host structures and by local stress heterogeneity.

Methods

Petrographic studies

Microscopic and scanning electron microscope (SEM) investigations of samples from mineralized quartz veins with visible areas of sulfide minerals helped to establish a paragenetic sequence of ore and gangue hydrothermal minerals. Samples with interesting microscopic features observed by optical microscopy were selected for additional SEM imaging by backscattered electron (BSE), cathodoluminescence (CL), and energy-dispersive X-ray spectroscopy (EDS) using a Zeiss EVO SEM with LaB6 electron source, housed at the Earth and Atmospheric Sciences, University of Alberta. CL imaging was done without applying a carbon coat as the SEM was operated in the variable low-pressure mode.

Geochronological studies of the host rocks

Zircon grains recovered from a 3 kg sample by conventional crushing, sieving, and heavy liquid separation

techniques were mounted on double-sided tape, cast in epoxy mounts and polished to expose their interiors. The polished mounts were then gold-coated and studied under a TESCAN VEGA2 scanning electron microscope (SEM) at the Department of Mineralogy and Petrology of Karlsruhe Institute of Technology (KIT), Germany. Subsequently, the gold coating was removed and U–Pb analysis performed by laser ablation-sector-field inductively coupled plasma mass spectrometer (LA-SF-ICP-MS) using a 193 nm ArF Excimer laser (Analyte Exite+, Teledyne Photon machines) coupled to Thermo-Scientific Element XR instruments at KIT. Analytical setups and measuring conditions are presented in Supplemental Table S1. All raw data were corrected offline using an in-house MS Excel © spreadsheet program (Gerdes and Zeh 2009), and applying a common Pb correction based on the interference and background-corrected ^{204}Pb signal and a model Pb composition (Stacey and Kramers 1975). Twenty four zircon grains from Gidami were analyzed during two sessions (three grains during session 1, and twenty-one during session 2) together with reference zircon GJ1#5 (primary standard during session 1; ID-TIMS of 604 ± 1.2 Ma in-house $^{238}\text{U}/^{206}\text{Pb}$ value of grain #5; unpublished); BB (primary standard during session 2; LA-ICP-MS of 561.6 ± 0.6 Ma; Santos et al. 2017), Plešovice (ID-TIMS age of 333.17 ± 0.18 Ma; Sláma et al. 2008), and KA1 of KaapValley granite (CA-ID-TIMS $^{207}\text{Pb}/^{206}\text{Pb}$ age of 3227.2 ± 0.2 Ma; Schoene et al. 2006). For results of standard measurements see Supplementary Table S2. The $^{207}\text{Pb}/^{235}\text{U}$ ratios were calculated using the corrected $^{206}\text{Pb}/^{238}\text{U}$ and $^{207}\text{Pb}/^{206}\text{Pb}$ ratios assuming a natural $^{238}\text{U}/^{235}\text{U}$ of 137.818. Uncertainty was obtained by quadratic addition of propagated errors on both ratios. Age calculations and data plotting were performed using the Isoplot toolkit (Ludwig 2008) v.4.15 for MS Excel©. The results of zircon U–Pb dating are listed in Supplemental Table S2.

$^{40}\text{Ar}/^{39}\text{Ar}$ geochronology of hydrothermal muscovite

Samples for $^{40}\text{Ar}/^{39}\text{Ar}$ dating were selected by petrographically-guided microsampling. First, polished thick sections (~500 μm thick) were prepared in Crystal-Bond 509 acetone-soluble thermoplastic and polished to a 1-micron finish with diamond suspension. The thick sections were then examined at the US Geological Survey Geology, Energy, and Minerals Science Center electron microbeam laboratory in Reston. Samples were analyzed using a Hitachi SU-5000 field emission scanning electron microscope (FE-SEM) fitted with a BSE detector, a Hitachi UVD detector that acts as panchromatic cathodoluminescence detector when operated at 0 V bias, and a 100 mm² Oxford Ultima energy-dispersive spectroscopy (EDS) silicon drift detector. Backscatter electron and cathodoluminescence imaging along with EDS of these

thick sections was used to document microtextural relationships and mineralogy and to select areas for $^{40}\text{Ar}/^{39}\text{Ar}$ micro-sampling. For some samples, a microdrill (manufactured by Ulrike Medenbach, Ruhr-University Bochum) mounted to an optical microscope was used to extract cores $\sim 300\text{--}500\ \mu\text{m}$ in diameter. Following BSE and CL imaging muscovite was separated from the polished thick sections of the studied samples using an Exacto knife. All samples were repeatedly ($3\times$) soaked for $> 1\ \text{h}$ in acetone to ensure complete removal of thermoplastic. The samples were then rinsed in a Branson 220 ultrasonic cleaner for 5 min each in acetone, ethyl alcohol, and then 3 times in deionized water prior to packing. The cores were packed in high purity copper, sealed under vacuum in fused silica vials, and irradiated for 40 MWH in the central thimble of the USGS TRIGA reactor in Denver, in a geometry similar to that described in McAleer et al. (2017). The sample assembly was rotated during irradiation to minimize the radial gradient in the fast neutron fluence and no cadmium shielding was used.

Following irradiation, all unknown samples were analyzed at the US Geological Survey Bascom Argon Dating (BARD) laboratory in Reston (Virginia). Samples were step-heated either in a low-blank furnace similar to that described by Staudacher et al. (1978) or via a defocused Synrad V30 series CO_2 laser, and argon isotopes were measured on a single collector VG-1200B mass spectrometer in peak hopping mode. The standard MMhb-1, with an age of $519.4 \pm 2.5\ \text{Ma}$ (Alexander et al. 1978; Dalrymple et al. 1981) was used to monitor the neutron fluence. Interfering isotope ratios were determined on co-irradiated CaF_2 and zero age K-glass. For data reduction the values of Lee et al. (2006) were used for the isotopic composition of air, and the decay constants of Steiger and Jäger (1977) were used to maintain consistency with an age of 519.4 for MMhb. Additional methodological details can be found in McAleer et al. (2017) and additional data reduction parameters as well as complete isotopic data can be found in the Supplemental Table S3 and Zoheir et al. (2022).

Microchemistry of pyrite

Pyrite grains were analyzed for their Fe, Cu, Co, Ni, As, and S contents using a JEOL JXA-8900R electron microprobe (EMPA) at the University of Kiel. Operation conditions were 20 kV and a beam current of 30 nA, and a spot size of $1\ \mu\text{m}$ and on-peak measurement times of 10–30 s. Off peak locations were analyzed for half the on-peak time. Natural and synthetic standard materials were used for external calibration. The detection limit is around 0.01 wt. % for all the measured elements.

Trace element concentrations in pyrite generations

Trace element concentrations of gold-associated pyrite were determined by an AGILENT 7900 s ICP-MS equipped with a GeoLas Pro HD laser ablation system at Kiel University. Ablation was done by using a laser beam energy of $2.6\ \text{J cm}^{-2}$, and analysis time was 90 s, of which 60 s of analysis with laser on and 30 s with laser off for background measurement. The employed spot size was $32\text{--}60\ \mu\text{m}$, at a pulse frequency of 5 Hz. A set of 21 isotopes was chosen for spot analyses: ^{52}Cr , ^{55}Mn , ^{57}Fe , ^{59}Co , ^{60}Ni , ^{63}Cu , ^{66}Zn , ^{75}As , ^{77}Se , ^{95}Mo , ^{107}Ag , ^{111}Cd , ^{120}Sn , ^{123}Sb , ^{125}Te , ^{182}W , ^{197}Au , ^{201}Hg , ^{205}Tl , ^{208}Pb , ^{209}Bi . The acquisition time for all masses was set to 0.02 s, with a total sweep time of $\sim 0.6\ \text{s}$. The graphical visualization tool of the GLITTER software package (van Achterbergh et al. 2001) was used for setting the integration intervals for each analyzed spot. The mass spectrometer was calibrated using calibration multi-element solutions and the NIST SRM-612 reference material. The internal standardization was based on ^{57}Fe concentrations determined by the EMPA. Two reference materials were used for external calibration: the USGS MASS-1 standard (Fe-Cu-Zn-S pressed powder pellet; Wilson et al. 2002) and the UQAC-FeS-1 synthetic versatile reference material from the LabMaTer (University of Quebec in Chicoutimi, Canada; Savard et al. 2018). All standards were analyzed at the beginning and at the end of each analytical session in order to monitor the sensitivity drift.

Analysis of fluid and mineral inclusions in vein quartz

Eight doubly polished thick sections ($\sim 100\ \text{mm}$ thick) were inspected using a custom-built Olympus BX53M petrographic microscope to identify and characterize fluid and mineral inclusions in the vein quartz. Sample petrography focused on identifying assemblages of fluid inclusions, their paragenetic context, and their phase assemblages at room-temperature. These results were used as a basis for subsequent microthermometric, Raman, and compositional analysis. Petrographic analysis also revealed that the vein quartz-hosted multiple mineral inclusions, and these were also characterized petrographically prior to Raman and SEM-EDS analyses.

Microthermometric analysis of fluid inclusions focused on petrographically determined fluid inclusion assemblages following the methods described by Goldstein and Reynolds (1994). Low-temperature microthermometry of fluid inclusions was conducted with a Linkam THMSG600 ($-100\text{--}600\ ^\circ\text{C}$) stage at the University of Alberta, calibrated using the triple point of CO_2 at $-56.6\ ^\circ\text{C}$, the triple point of H_2O at $0.0\ ^\circ\text{C}$, and the critical point of H_2O

at +374.1 °C. Estimated precision and accuracy of the temperature measurements is ± 0.1 °C at subzero temperatures and ± 0.5 °C at temperatures > 100 °C.

Raman spectroscopic analysis of fluid and mineral inclusions was done using a Horiba LabRam HR Evolution Raman microscope at the University of Alberta, using a 532 nm laser focused through a 100× objective lens. All spectra were acquired on unoriented grains using a laser power of 100 mW and two to three, 5–20 s exposures summed to the final reported spectra. Spectra were interpreted using the RRUFF database of Lafuente et al. (2016) for mineral species and Frezzotti et al. (2012) for fluid species.

Backscattered electron images, and elemental EDS maps were used to characterize the compositions of mineral inclusions and daughter phases in fluid inclusions which had been exposed during sample polishing. The BSE images and EDS maps were collected using a Zeiss EVO SEM with a LaB6 electron source at the University of Alberta. Acceleration voltage was set to 15–25 kV with a 300–500 pA beam current, and a 7–8.5 mm working distance. Images were collected in variable-pressure mode with a 100-mm aperture using collection times that varied between 1–15 min. All analyzed samples were uncoated. Lower accelerating voltages (15–20 kV) were used during EDS point analysis to reduce interference from the host quartz.

Results

Host rock geology and zircon U–Pb data

Gold-bearing quartz veins in the Gidami mine are hosted by variably deformed tonalite-trondhjemite rocks, as parts of a weakly foliated (WNW-ESE) massif of TTG rocks (Fig. 2B). These TTG rocks were differentiated from basic metavolcanic successions in the Qusseir sheet of the 1: 500,000 Conoco Coral (1987) maps. At the outcrop scale, the tonalite-trondhjemite rocks are coarse- to medium-grained and exhibit granular or porphyritic textures with sodic plagioclase and quartz as main constituents. Interlocking tabular plagioclase with resorption borders and irregular and granophyric intergrowths of plagioclase and quartz are commonly observed, though shearing and alteration locally obliterated the original igneous textures. Intense shearing and mylonitization along ~N-S shear zones are manifested by pervasive mortar and porphyroclastic textures. Minor biotite and rare hornblende are replaced by chlorite in some samples. Rare microcline forms irregular interstitial grains or occurs as fine inclusions. Oligoclase forms large laths and shows variable brittle and ductile microstructures, with microfractures that are filled partially with calcite. Titanite, apatite, and zircon are accessory minerals.

Zircon grains recovered from a least altered sample of the host granitoid rock adjacent to the main vein show a consistently short prismatic morphology, and are variably fractured. Well-developed concentric oscillatory zoning was observed in some zircon crystals, whereas relict of patch or irregular zoning characterized other zircon grains/fragments. Signs of alteration and core-rim relationships are generally absent.

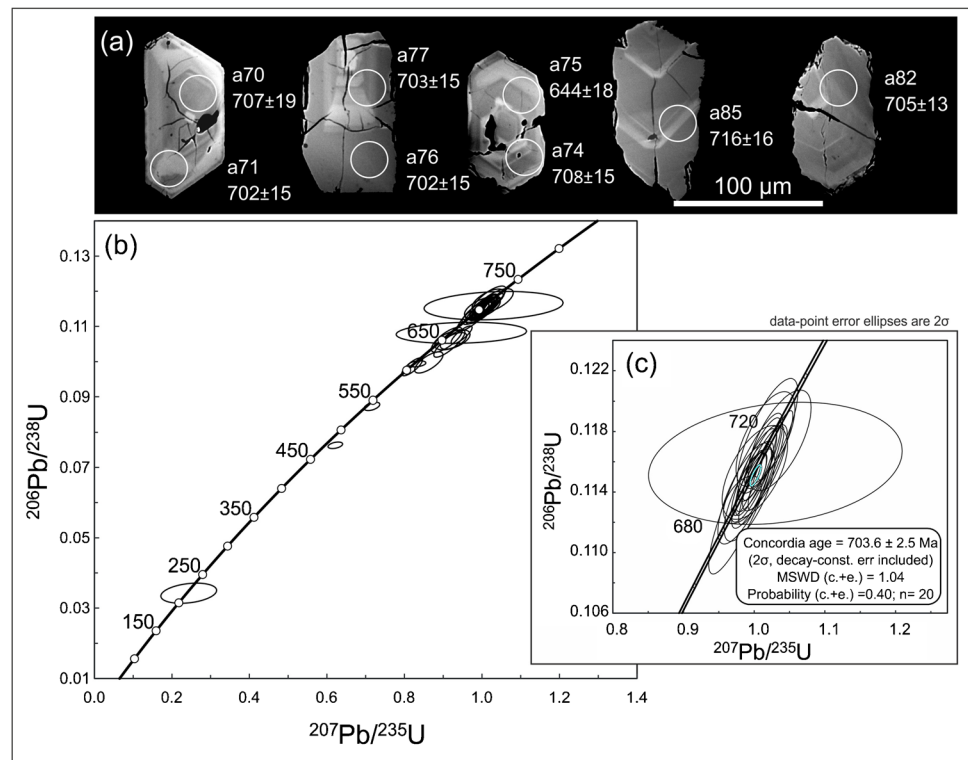
U–Pb isotopic data for the twenty four analyzed zircon grains are listed in Supplemental Table 2A and are plotted on Concordia diagrams (Fig. 3A, B). The recovered zircon grains have U concentrations varying from 29 to 573 ppm, and Th/U ratios of 0.20–1.02 (average 0.47, $n=32$). Most zircon analyses (20 out of 32) show low common Pb ($f_{206}\% \leq 2.0$, where f_{206} represents the proportion of common Pb relative to the total ^{206}Pb), and the remaining, mostly such derived from zircon domains with low U contents, higher values up to $f_{206}\% = 8.1$. The 20 oldest zircon domains yielded a concordant age of 703.6 ± 2.5 Ma (2σ , MSDW of concordance + equivalence = 1.04, Prob. of concordance + equivalence = 0.40; Fig. 3C), which is interpreted to date magma crystallization of the host rock. The remaining 12 analyses, mostly derived from low U-domains with relatively high Pb level, gave younger $^{206}\text{Pb}/^{238}\text{U}$ ages (mostly discordant), ranging between ~665 and ~220 Ma. These are interpreted to result from multiple Pb loss, perhaps related to subsequent tectonic and hydrothermal overprint(s).

The auriferous quartz veins: microstructural and mineralogical characteristics

The mineralized vein samples contain anhedral quartz and abundant coarse-grained muscovite that commonly form well-defined bands. Within individual bands, quartz occurs as masses of anhedral crystals surrounded by coarse muscovite and shows textures indicative of repeated fracturing and recrystallization during progressive deformation from plastic distortion to brittle destruction. Asymmetric quartz crystals define a sinistral sense of shearing (Fig. 4A, B). Coarse-grained muscovite veins and alteration occur both in the highly deformed wallrock and within the quartz veins. In the mineralized quartz veins, muscovite intergrowths with recrystallized quartz form patches or occupy anastomosing microshears with recrystallized quartz plus scattered fluorite, rutile and calcite, forming dark seams (Fig. 4C, D). Subgrain development and serrate quartz boundaries characterize the gold-sulfide quartz veins. Free gold blebs are located along the newly formed grain and phase boundaries.

Muscovite occurs throughout the veins, ranging from interstitial material between quartz grains, through clots of interlocking fibers, to large single plates or books (Fig. 4C, D). In detail, the muscovite-rich zones within quartz veins are characterized by fine-grained disseminations of calcite and fluorite that commonly appear to have been deposited

Fig. 3 Results of zircon U–Pb dating of the Gidami trondhjemite. (A) SEM-BSE images of the analyzed zircons with laser spot positions for U–Pb analyses. Numbers represent ^{206}Pb - ^{238}U ages. (B) A (Wetherill) Concordia diagram showing all results of U–Pb zircon dating. (C) Concordant age of the Gidami host rock based on 20 zircon spot analyses. MSWD, mean squared weighted deviation; Prob., probability; (c.-e.), of concordance and equivalence



relatively late in the paragenetic sequence, infilling between quartz grains and in some cases deposited along healed fractures that cut earlier quartz.

Quartz in the veins commonly shows evidence of reopening with multiple generations of crosscutting healed fractures evident in CL (ESM Fig. S1A–C). Notably, where muscovite and calcite appear to be surrounded by quartz in plane-polarized light and BSE images, the CL generally reveals that these latter minerals were deposited in healed fractures and thus postdate the bulk of quartz deposition (ESM Fig. S1C).

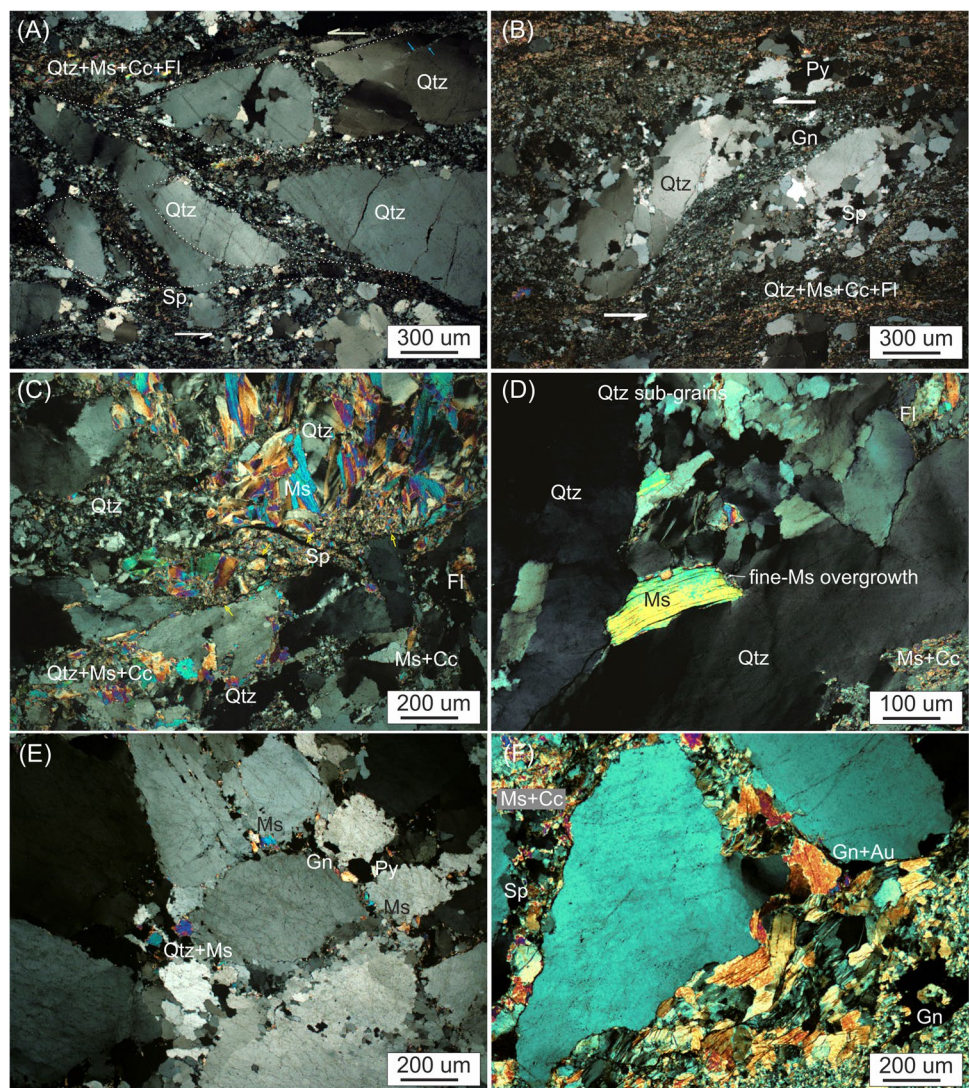
The early-formed quartz in the veins hosts abundant needle-like mineral inclusions that show high Ti in SEM–EDS analysis and show Raman spectra indicative of anatase (TiO_2 ; Fig. 5A–D). Owing to the acicular habit, we infer that the original rutile needles that underwent crystallographic transformation to anatase as a result of cooling and decompression (McNicoll et al. 2014). These needles occur mostly as elongate (10–30 µm), acicular crystals that are disseminated throughout the host quartz and resemble rutile exsolved from quartz, indicative of elevated TiO_2 concentrations in the quartz at the time of deposition. The quartz also hosts a subordinate population of micron-scale, platy inclusions, which show EDS peaks for Al, K, and Fe (Fig. 5D), and were confirmed as muscovite by Raman spectroscopy (Fig. 5C).

Ore microscopy indicates that pyrite is ubiquitous in the gold-bearing quartz veins and in the altered wallrock.

Pyrite occurs as subhedral crystals with discrete pyrrhotite, arsenopyrite and silicate inclusions. Based on the variable morphological and textural features, three generations of pyrite were identified (PyI, PyII, and PyIII) (Fig. 6A–C). PyI forms porous cores of subhedral grains that are surrounded by inclusion-free margins of PyII (Fig. 6A, B). Discrete subhedral grains of PyII and PyIII are commonly deformed and locally replaced by galena, sphalerite, and gold along microfractures (Fig. 6D–H). Arsenopyrite occurs as sparse euhedral crystals in large PyII crystals. Galena replaces pyrite and forms intergrowths with hessite and locally cervelleite along fractures in PyII (Fig. 6D). Sphalerite and chalcopyrite occur as patchy replacements or infillings among deformed pyrite crystals (Fig. 6E). Gold in quartz veins is commonly associated with galena and sphalerite along microfractures in quartz and pyrite crystals. Chalcopyrite is partially replaced by covellite, particularly in the sulfidized wallrock.

Textural relationships indicate that pyrite, pyrrhotite, and less common arsenopyrite were related to an early paragenetic ore stage (Fig. 7). Continued pyrite precipitation, most likely under different depositional conditions, led to the formation of inclusion-free pyrite (PyII) surrounding the earliest pyrite generation (PyI). The early pyrite was replaced in part by late-paragenetic galena, sphalerite, and chalcopyrite, and microfractures in the early formed pyrites were healed by a late pyrite generation (PyIII). The dispersed gold, hessite, and cervelleite specks are attributed to the latest stage of sulfide-gold mineralization in the Gidami deposit (Fig. 7).

Fig. 4 Deformation features in the gold-sulfide quartz veins from the Gidami deposit. **A, B** Saccharoidal quartz along shears dissecting the large quartz crystals (Qtz). Notice that the braided sets of microfractures depict a sinistral sense of shearing and are healed by microcrystalline quartz (Qtz) + muscovite (Ms) + calcite (Cc) + fluorite (Fl), and less commonly by pyrite (Py) and sphalerite (Sp). **C, D** Muscovite intergrowths with microcrystalline quartz, and fine-grained muscovite-calcite-fluorite mixtures fill late microfractures. Notice the sub-epitaxial overgrowths of fine-grained muscovite on a coarse-grained muscovite flake, particularly adjacent to the microcrystalline quartz. **E, F** Muscovite, microcrystalline quartz and galena (Gn) associated with serrate quartz grains or developed along the crosscutting microfractures. In rare cases, galena and gold (Au) occur at the contact between muscovite and irregular quartz grains



$^{40}\text{Ar}/^{39}\text{Ar}$ ages of hydrothermal muscovite

To constrain the age of mineralization, we applied $^{40}\text{Ar}/^{39}\text{Ar}$ geochronology to muscovite disseminated in quartz-gold veins and in an altered host rock sample. Optical and electron petrography were used to determine the petrogenetic relationship of the dated muscovite to mineralization—and microsampling (see “Methods”) was used to maintain the petrologic context of the dated samples. The petrologic context and the $^{40}\text{Ar}/^{39}\text{Ar}$ data for each sample are presented below.

Sample GD-21 (26° 23' 08" N, 33° 27' 12" E) was collected from the contact of a gold-bearing quartz vein and altered wallrock. At the vein-wallrock contact, three mineralogical zones were identified (Fig. 8). Zone 1 extends for the first several millimeters adjacent to the contact and is composed of contact-parallel zones of nearly pure coarse-grained muscovite and quartz. Also present in this zone

are ~10- μm -thick fluorite veins that cut quartz and locally some coarse-grained muscovite. Muscovite is randomly oriented and exhibits some minor zoning in BSE imaging and EDS analysis, reflecting variations in Mg/Fe ratios (Fig. 8C). Zone 2 extends for the next ~1 cm away from the contact and is composed of fine-grained disseminated fluorite in a matrix of fine-grained muscovite along with minor monazite and rutile, Mn + Zn-bearing ilmenite, and ecandrewsite intergrowths. In this zone, euhedral terminations of muscovite can also be found in rare coarse-grained fluorite (Fig. 8E). Farther from the contact (Zone 3), biotite is present and the wallrock is comprised of disseminated fluorite in a matrix of fine-grained muscovite, quartz, and biotite, again with minor rutile, Mn + Zn-bearing ilmenite, and ecandrewsite intergrowths (Fig. 8E, F). The textural association of fluorite, Zn-ilmenite, and biotite in this zone indicates that fluorite and Zn-ilmenite replace biotite, and we suggest that this replacement went to completion in Zone 2. Field relations

Fig. 5 Submicroscopic mineral inclusions in quartz veins. **A** Transmitted light photomicrograph (PPL) showing acicular TiO_2 crystals (as well as some carbonic fluid inclusions) hosted in quartz. **B** High-magnification view (left=plane polarized light; right=BSE) of a TiO_2 needle as well as a platy grain of muscovite hosted in quartz. **C** Raman spectra of mineral inclusions shown in A and B (indicated by the arrows), showing the characteristic peaks of anatase and muscovite. **D** SEM-EDS maps of same field of view shown in B, showing peaks for Ti in an anatase needle, and for Al, K, and Fe in a muscovite grain

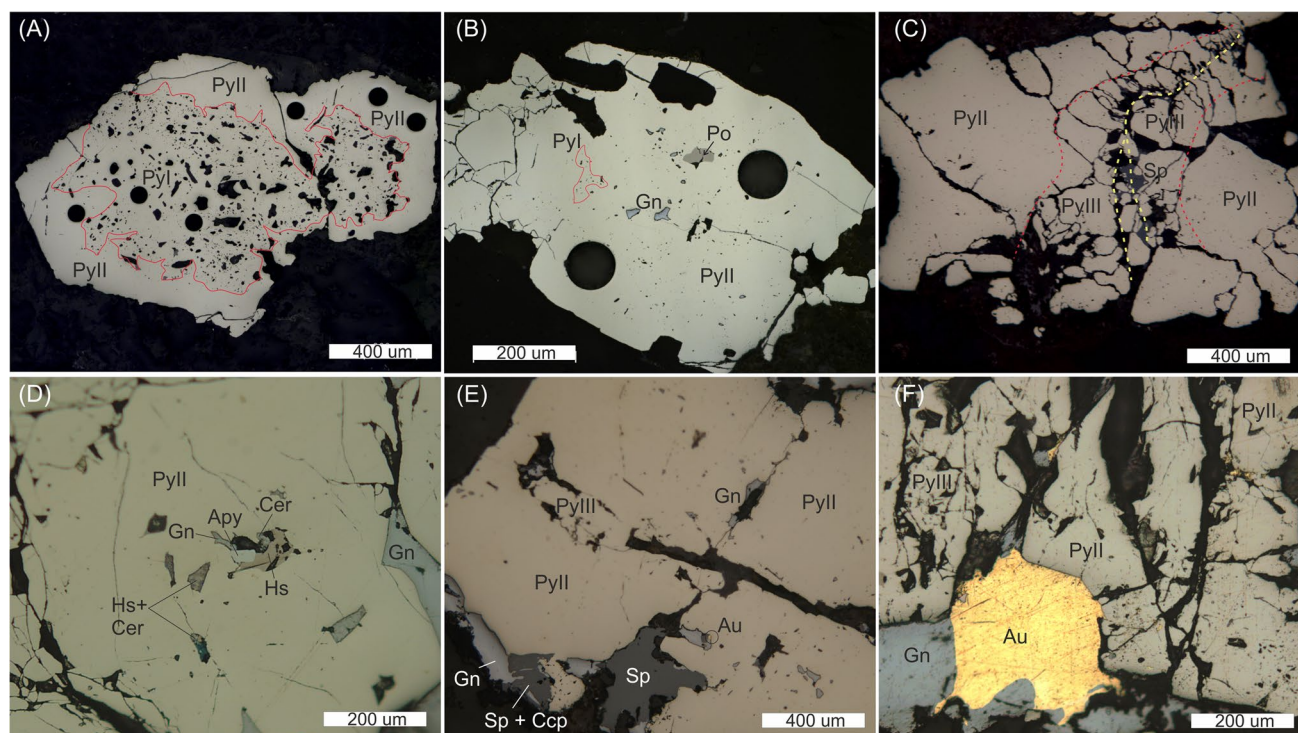
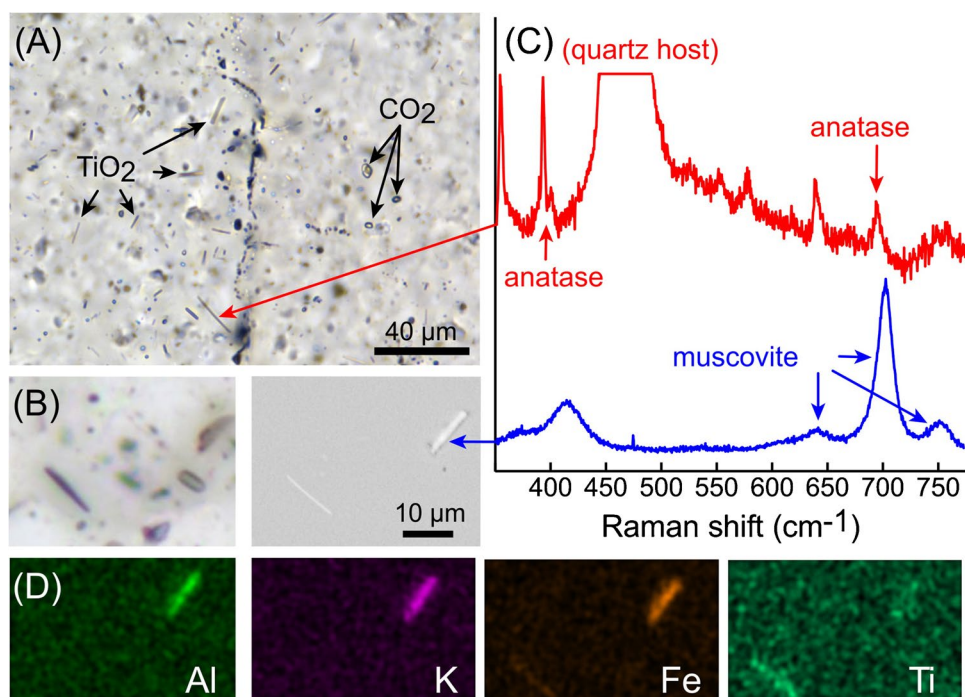


Fig. 6 Mineralogy and ore textures of the Gidami gold deposit. **A** Porous pyrite (PyI) surrounded by massive pyrite zones (PyII). **B** Pyrrhotite (Po) and galena (Gn) inclusions in a PyII subhedral crystal. **C** PyIII is confined to a microfracture in a large PyII crystal. **D**

Arsenopyrite (Apy) and pyrrhotite inclusions in PyII, and galena filling crosscutting fractures. **E** PyIII along fractures PyII, and galena-sphalerite-chalcopyrite replacing PyII. **F** Gold (Au) intergrowth with galena along fractures in PyII

Fig. 7 Paragenetic sequence of gold-sulfide mineralization at the Gidami deposit and related hydrothermal alteration phases

<i>Mineral Phase</i>	<i>Early Stage</i>	<i>Late Stage</i>
Quartzcoarse.....sub-grain, comb.....
Muscovite	
Carbonate	
Fluorite	
Ecandrewsite (Zn-ilmenite)	
PyritePyI.....PyII.....PyIII.....
Arsenopyrite	
Sphalerite	
Galena	
Chalcopyrite	
Pyrrhotite	
Hessite	
Cervelleite	
Gold	

indicate that the protolith of this metasomatized wallrock is trondhjemite, with major oligoclase, minor K-feldspar and rare biotite as relict of the original igneous assemblage. Hydrothermal K-feldspar is locally present as overgrowths on the altered oligoclase crystals.

Sample GD-35 (26° 23' 20" N, 33° 27' 09" E) is a quartz vein from the northern part of the main vein with muscovite patches and fracture-controlled dissemination of fluorite (ESM Fig. S2A). Muscovite occurs as coarse (> 500 µm), randomly oriented grains and as finer disseminated grains in the quartz matrix. The coarse grains show some zoning in BSE imaging and EDS analysis shows this is caused largely by variations in Fe/Mg (ESM Fig. S2B). Muscovite is cross-cut by fluorite veinlets (ESM Fig. S2C) but locally has euhedral terminations in coarse fluorite (ESM Fig. S2D). Fluorite occurs as coarse grains and forms veins cutting or replacing muscovite. These textural relationships suggest that fluorite post-dates most muscovite growth.

Sample GD-32 (26° 23' 28" N, 33° 26' 57" E) is a quartz-muscovite vein from the northern quartz vein swarms with veinlets of fluorite. An ~ 3 cm × 1 cm fragment composed of rutile, Mn + Zn-bearing ilmenite, and ecandrewsite intergrowths in a matrix of fine-grained muscovite occurs within quartz (ESM Fig. S3A-D). This fragment is surrounded by coarse-grained muscovite and lesser coarse-grained fluorite (ESM Fig. S3B, C). The mineralogy and texture are similar to that observed at the vein-wall contact in sample GD-21 and suggests that this fragment may be altered wallrock material.

Sample GDg (26° 23' 36" N, 33° 27' 07" E) is a muscovite-calcite altered wallrock adjacent to the northern extension of the main quartz vein. It is comprised mainly of muscovite, quartz, calcite, K-feldspar, and iron oxides,

with minor fluorite, apatite, manganese oxides, and zircon (ESM Fig. S4A-D). Intergrowths of muscovite and quartz are here interpreted to be hydrothermal. Muscovite occurs in masses of fine-grained randomly oriented crystals. These can be nearly monomineralic but can also be found with apatite and fluorite inclusions. Locally euhedral muscovite can be found terminated in coarse fluorite as was observed in GD-21 and GD35. Calcite forms late veins that crosscut most of the other mineralogy (ESM Fig. S4D).

A furnace step-heating experiment on a 0.113 mg aliquot from sample GD-21 yielded an age spectrum with anomalously old ages in early steps, followed by a plateau age of 584.0 ± 3.1 Ma (2σ), that includes 70.9% of the ^{39}Ar and has an MSWD of 0.14 (Fig. 9A). Coarse-grained muscovite was microdrilled from sample GD-35 and dated. A furnace step heating experiment on a 0.125 mg aliquot yielded a plateau age of 582.0 ± 3.7 Ma (2σ), which includes 10% of the ^{39}Ar and has an MSWD of 0.52 (Fig. 9B). Fine-grained muscovite, intergrown with minor fluorite and Mn + Zn-bearing ilmenite, was microdrilled from sample GD-32 and dated. A laser step heating experiment on a 0.154 mg aliquot is slightly discordant and did not yield a plateau age. The weighted average age, including all steps, is 584 ± 4 Ma (2σ), has an MSWD of 5.8, in general agreement with the other samples (Fig. 9C). Fine-grained muscovite in sample GDg was microdrilled from localities with the fewest inclusions, and where no K-feldspar was present. A furnace step heating experiment on a 0.193 mg aliquot yielded an age spectrum with anomalously young ages for the first 5% of gas release. The remainder of the age steps fall between 572 and 582 Ma, and define a plateau age of 581.5 ± 3.1 Ma (2σ), that includes 52.9% of the ^{39}Ar and has an MSWD of 0.75 (Fig. 9D).

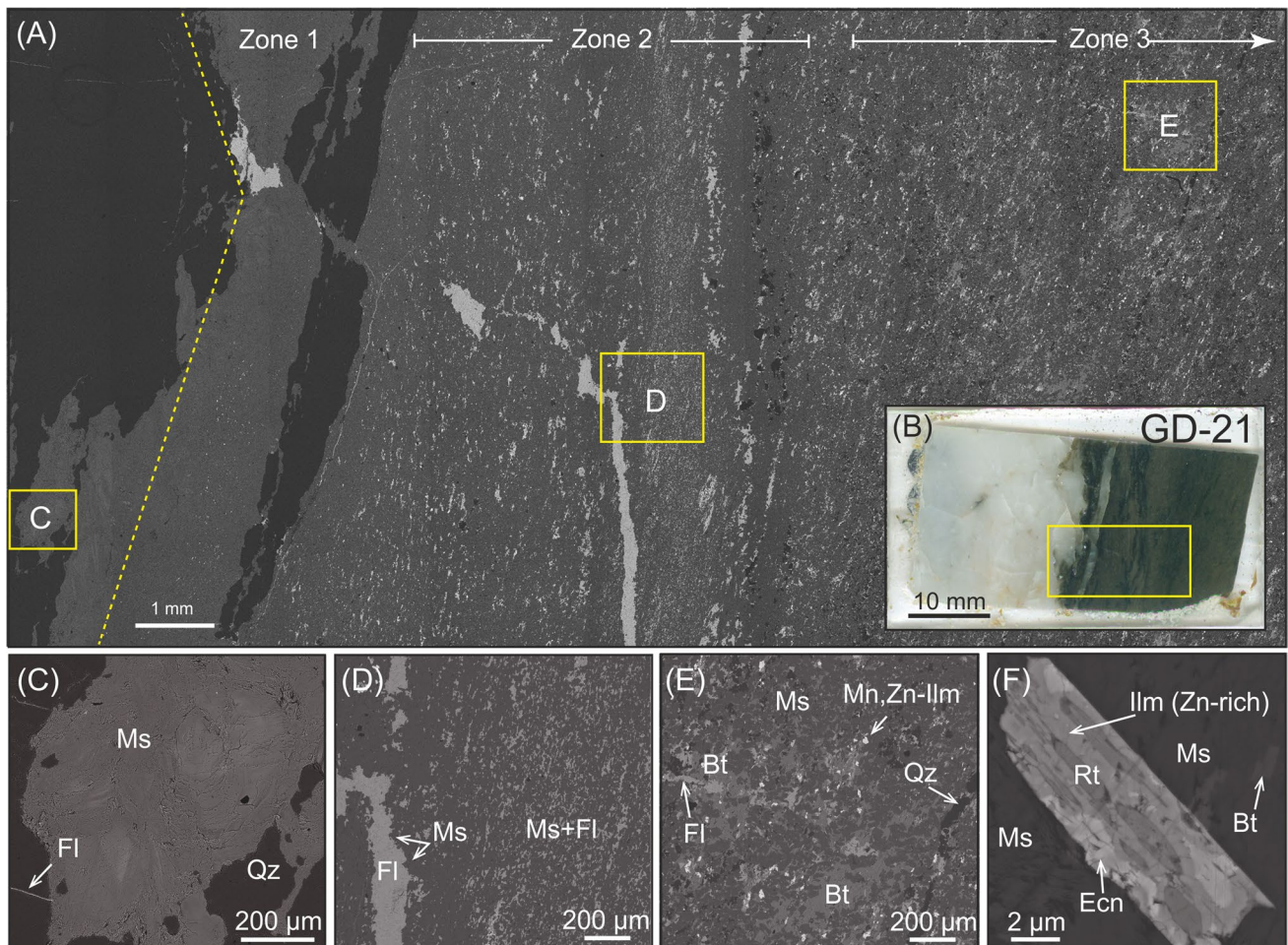


Fig. 8 (A) BSE image of sample showing mineralogical zones discussed in text. Dashed yellow line is approximate exact knife cut for sampling coarse muscovite. (B) Polished thick section of GD-21 prior to micro-sampling. (C) Zone 1 composed of coarse-grained muscovite with thin fluorite veinlets. (D) Zone 2 composed dominantly of

disseminated fluorite and fluorite veins in a fine-grained muscovite matrix. (E) Zone 3 with biotite, quartz, Mn-Zn rich ilmenite in addition to disseminated fluorite and fine-grained muscovite. (F) Image showing “Mn-Zn ilmenite” is composed of ecandrewsite (Ecn), Zn-rich ilmenite, and rutile

Textural and microchemical characterization of pyrite generations

Confirming the microscopic observations, SEM – BSE imaging of the sulfide-rich quartz vein samples reveals three pyrite varieties (PyI, PyII, and PyIII) with distinct morphological and microtextural relationships. PyI corresponds to uncommon porous zones in some large grains (Fig. 10A), with high Pb contents and variable As concentrations but generally < 1 wt.% (Supplemental Table S4). PyII occurs as overgrowths surrounding PyI, with complex internal structures and oscillatory or boxwork (cross-hatched) zoning patterns (Fig. 10A, B). Arsenic concentration in PyII is variable, but commonly > 1 wt.%. The EPMA data of PyII reveal an antithetical relationship between As and S for analyses with > 1 wt.% As. PyIII forms late blocky and elongate grains interlocking in a comb texture along fractures

or occurs as non-epitaxial overgrowths on earlier pristine pyrite (Fig. 10C, D).

In the SEM-BSE images, small galena inclusions scatter preferentially within patchy dark areas in otherwise bright PyII (Fig. 10A, D, dashed yellow areas), and decorate grain boundaries in PyI and PyII (Fig. 10C, red arrows). Gold also occurs locally in these areas (Fig. 9C, black circles). Galena inclusions can also be found along the medial line of syntaxial veins comprised of comb PyIII (Fig. 9C, black double-headed arrow). Finally, fine and coarse-grained galena along with sphalerite and gold commonly occur along fractures that crosscut PyIII.

Representative ablation time-resolved depth profiles for different varieties of pyrites from the Gidami deposit are shown in ESM Figure S5. PyI shows trace element patterns that have spiky signals for Pb, Bi, Ag, Cu, Te, Sb, and Au, and locally show very high values (> 10⁴ counts per second,

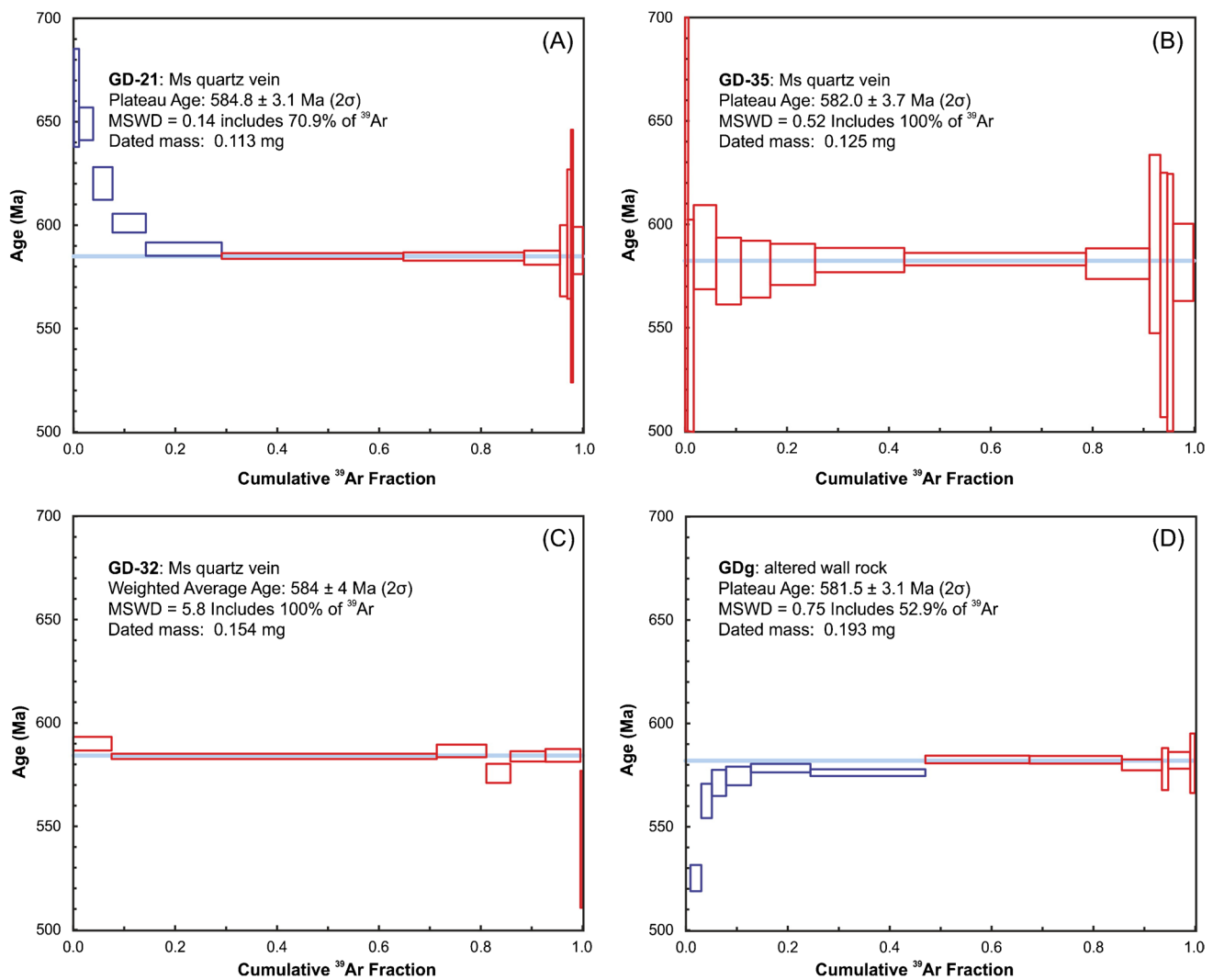


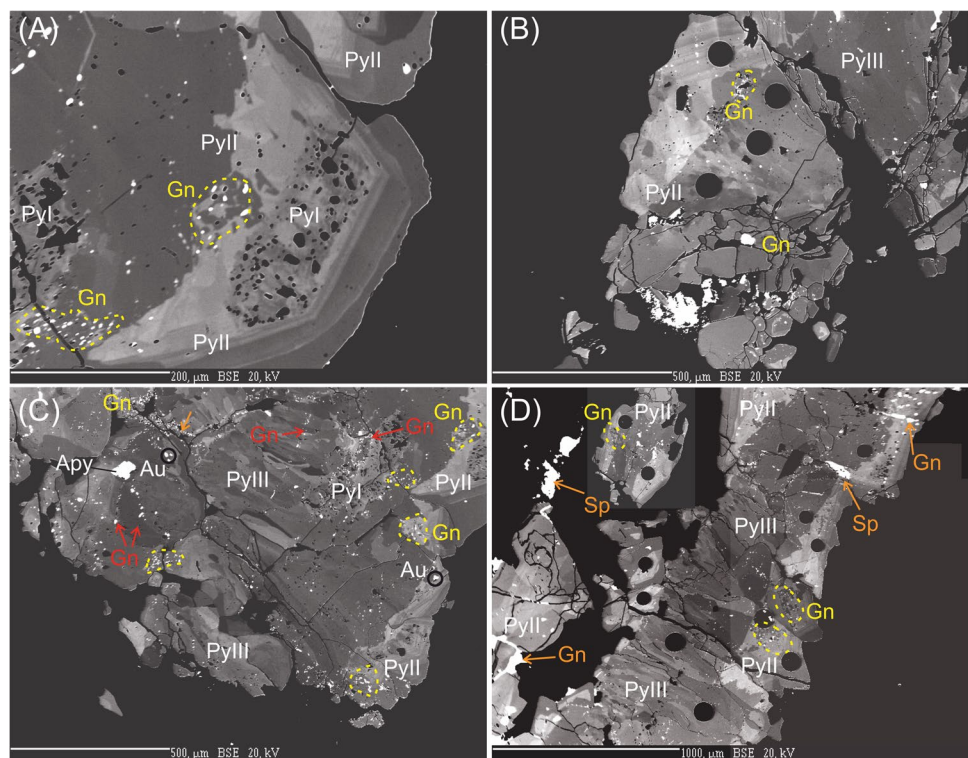
Fig. 9 Age spectra from four samples from the Gidami Au deposit, included 3 muscovite samples from Qtz-Au veins and 1 sample of altered wall rock. All samples yield ages that agree at 2σ at ~ 583 Ma

cps), most likely related to buried submicroscopic mineral inclusions. Considerably elevated Au signals $> 10^6$ cps characterize spots with noticeable As enrichments. PyII is characterized by consistently high-level and steady signals for As, Co, and Ni, and the Au signal remains smooth at a relatively high counts rate ($> 10^4$ cps $\cong 2$ ppm) (ESM Fig. S5). Elevated Au signals are accompanied by detectable Pb, Ag, Bi, Te, and Sb in some analyses. PyIII patterns are characterized by high-level signals for Sb, Ni, and Pb, commonly at 10^6 cps. Bi, Cu and Sb abundances in PyIII are relatively high compared to PyI and PyII varieties as indicated by their signals at 10^5 cps (ESM Fig. S5). The Au signals in PyIII are below the background level, but variations in Au count rate generally correlate with high As spectra ($> 10^6$ cps).

Data from LA-ICP-MS spot analyses on the different stages of pyrite grains from the Gidami deposit are given in Supplemental Table S5. PyI contains variable

concentrations of As (9 to 3988 ppm), Co (2 to 662 ppm), Ni (3 to 1564 ppm), Zn (< 1 to 525 ppm), Ag (~ 1 to 42 ppm), Pb (16 to 9180 ppm), Bi (~ 3 to 347 ppm), and Au (< 1 to 8.4 ppm). The trimmed mean (0.2 = 20% proportional cut of outlier values) for As is 402 ppm, Ag 9.6 ppm, and Au is 2.1 ppm. PyII is characterized by irregular but mostly elevated concentrations of As (7.2 to 13,256 ppm) and Au (0.1 to 7867 ppm) with high trimmed means (0.2) of 3045 ppm and 60.5 ppm, respectively. Other chemical characteristics of PyII include consistent and high concentrations of Co (trimmed mean 0.2 = 376 ppm), Ni (trimmed mean 0.2 ≈ 101 ppm), Ag (trimmed mean 0.2 ≈ 101 ppm), Pb (trimmed mean 0.2 ≈ 280 ppm), and Bi (trimmed mean 0.2 ≈ 47 ppm). Noticeably, Au content increases as concentrations of Pb, Bi, Ag and Sn increase, suggesting a micro-inclusion mode of occurrence at least for some spot analyses. PyIII is

Fig. 10 Back-scattered electron (BSE) images showing features of pyrites from the Gidami gold deposit. **A** PyI forming porous zones in PyII zoned subhedral crystals with locally scattered intrusions of galena (Gn). **B** PyII grain showing cross-hatching zoning and brittle deformation at margins. **C** PyII zoned crystal cut by a median line microfracture that was healed by comb PyIII elongate crystals, note the trail of galena orthogonal to the long-axis of the pyrite (black double-headed arrow). Also seen is an inclusion of arsenopyrite (Apy) and dispersed gold (Au) particles (black circles). **D** PyII vein reopened and filled with PyIII interlocking grains. Galena and sphalerite (Sp) heal microfractures in sulfide grains and the vein quartz. For additional details, see text



distinctly poor in Au (generally < 1 ppm) and in many other trace elements (e.g., Ag, Co, Zn, and Cu). Pb, Ni and Bi concentrations are relatively high in this pyrite variety, with trimmed means $0.2 \approx 1029$ ppm, 132 ppm, and 58 ppm, respectively. Signal fluctuations suggestive of buried micro-inclusions are much less common in PyIII, as also revealed by the mostly smooth spectra in the time-resolved depth profiles, relative to PyI and PyII varieties.

As shown in Fig. (11A), the collected LA-ICP-MS data from the three pyrite varieties suggest significant variations in the Au/As atom ratio among and within each pyrite generation in the Gidami deposit. The Au/As ratios obtained from most analyses vary from 1:100,000 to near 1:10 (in mol%), corresponding to a change in this ratio of up to four orders of magnitude. Despite that fact that these values plot consistently below the maximum solubility limit of Au in pyrite (Reich et al. 2005), such magnitude of change is most likely related to Au occurring as nanoparticles rather than in solid solution within the pyrite crystal lattice (e.g., Deditius et al. 2014). The Au contents show a clear positive correlation with Ag and Sb in all pyrite varieties, where PyI occupies the intermediate position between PyII and PyIII (Fig. 11B–F). PyIII is consistently poor in most trace elements, whereas PyI and PyII have nearly overlapping concentrations of many trace elements, e.g., Bi, Zn, and Pb (Fig. 11D–F).

Fluid inclusions

Vein quartz at Gidami is densely inundated with carbonic-aqueous fluid inclusions (Fig. 12A, B; results summarized in Supplemental Table S6). Based on petrographic analysis, the fluid inclusions are secondary or of uncertain origin, whereas unambiguous primary fluid inclusion assemblages were not observed. The fluid inclusions range from equant shapes through to highly irregular ones. As also observed in previous studies (Zoheir et al. 2019a, b, c), the texturally best-preserved fluid inclusions with equant shapes are most commonly observed in quartz grains that are partially sheathed by, or in close proximity to, sphalerite, and such inclusions are invariably either three-phase (liquid–liquid–vapor) carbonic-aqueous inclusions with double bubbles or apparently monophasic carbonic inclusions that appear dark (in some cases, opaque) in transmitted light. The latter two types are commonly observed together in the same clusters and assemblages. Elsewhere in the recrystallized quartz throughout the veins, partially decrepitated inclusions consisting of dismembered cores surrounded by small neocate inclusions (Tarantola et al. 2010, 2012) are commonly observed (Fig. 12A, B).

The presence of CO₂ in the carbonic-aqueous inclusions is indicated by the double bubbles as well as the ubiquitous observation of “double freezing” (i.e., solidification of clathrate, followed by solidification of dry ice) during

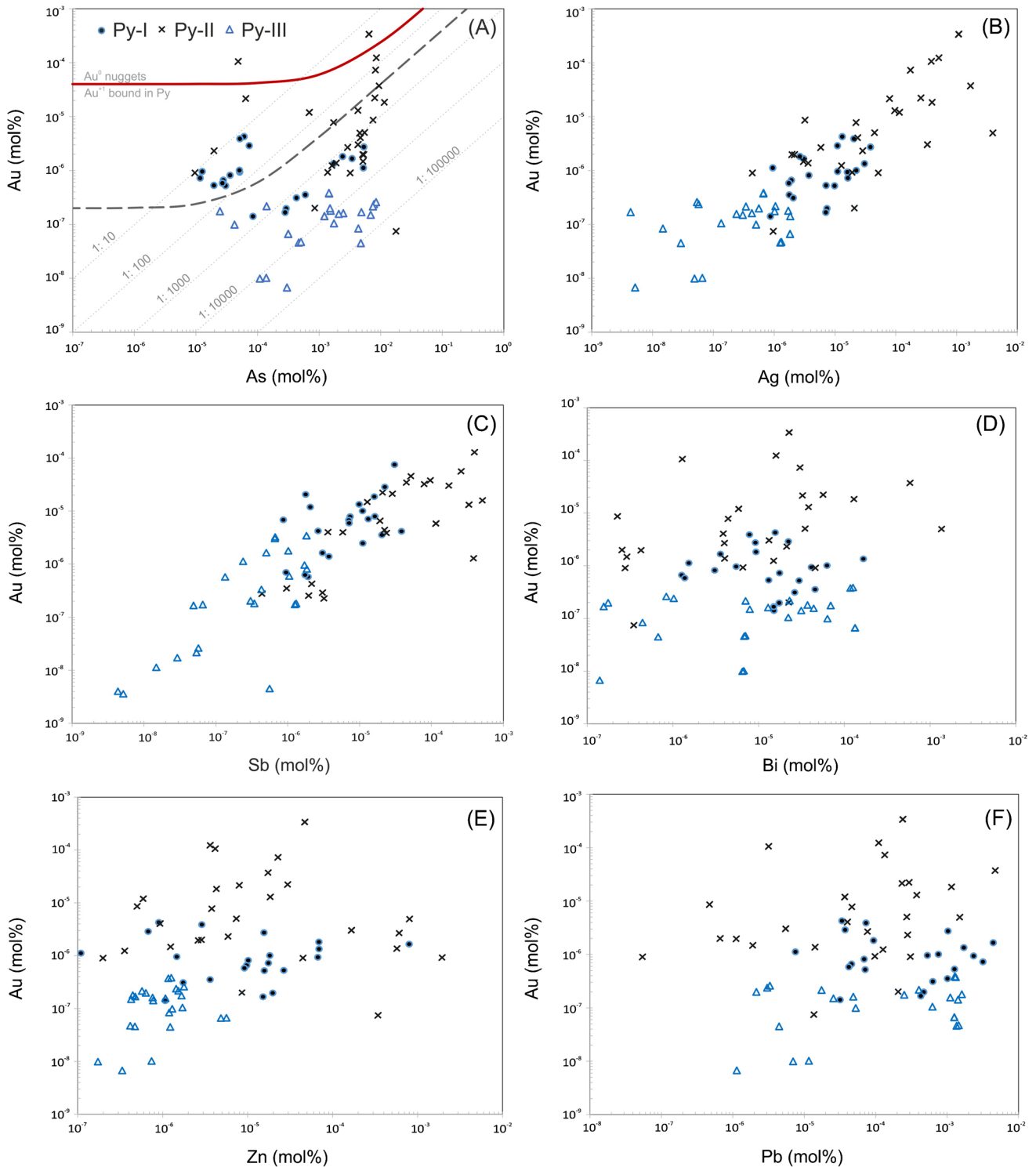


Fig. 11 Logarithmic plots of Au vs. As (A), Ag (B), Sb (C), Bi (D), Zn (E) and Pb (F) for the three pyrite varieties in the Gidami gold deposit. Red thick curve in (A) is the solubility limit of Au in As-pyrite ($C_{Au} = 0.02 \times C_{As} + 4 \times 10^{-5}$) as suggested by Reich et al.

(2005). The broken line marks the maximum solubility limit of Au in pyrite ($C_{Au} = 0.004 \times C_{As} + 2 \times 10^{-7}$) from orogenic gold deposits (from Deditius et al. 2014). Dotted lines in (A) represent Au:As ratios (log-scale, in mol%)

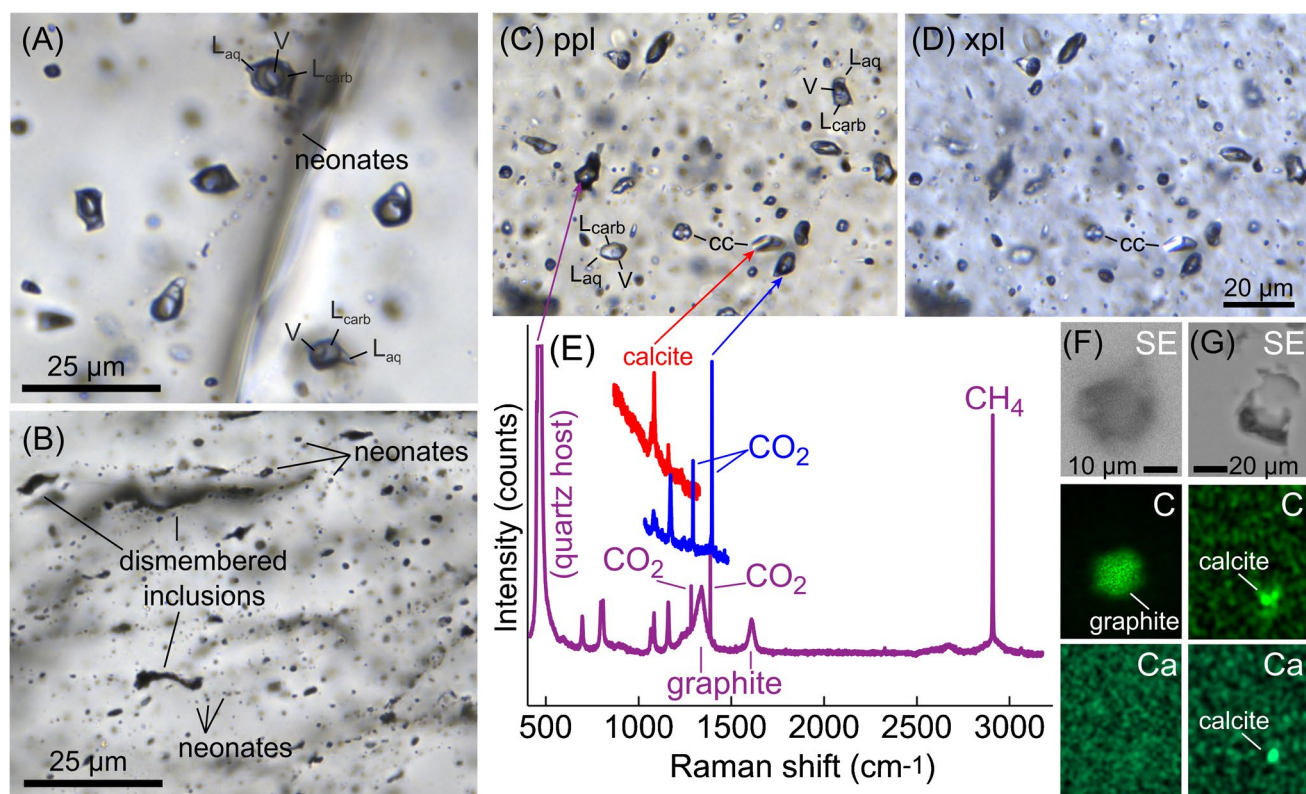


Fig. 12 (A) and (B) Photomicrographs of quartz-hosted fluid inclusion assemblages. (A) Assemblage of three-phase carbonic-aqueous inclusions; L_{aq} = aqueous liquid; L_{carb} = carbonic liquid; V = vapor. (B) Assemblage of partially decrepitated inclusions consisting of dismembered cores surrounded by small neonates (Tarantola et al. 2010, 2012). (C)–(G) Analysis of fluid inclusions of different types. (C) and (b) Cluster of fluid inclusions showing several three-phase carbonic-aqueous inclusions (labels as in A, B), two inclusions with obvious birefringent grains (as seen in cross-polarized light, D), as well as

several apparently monophasic, dark carbonic inclusions. (E) Raman spectra of several inclusions shown in C and D, showing CO_2 in the carbonic-aqueous inclusions; calcite in the inclusions that host birefringent grains; and CO_2 , CH_4 and graphite collectively in the apparently monophasic carbonic inclusions. (F) and (G) SEM secondary electron images and corresponding EDS element maps of breached inclusions, showing a peak for carbon in a graphite-bearing inclusion (F), and peaks for calcium and carbon in a calcite-bearing inclusion (G)

cooling to $-150\text{ }^\circ\text{C}$, and by consistent melting behavior at $-56.6 \pm 1\text{ }^\circ\text{C}$ during low temperature microthermometry. The presence of CO_2 is also confirmed by the Raman spectroscopic analyses that show the characteristic Fermi diad of CO_2 (Fig. 12C–E). During microthermometry, the carbonic fluid portion consistently homogenized to the liquid phase at $25\text{--}30\text{ }^\circ\text{C}$. However, additional heating resulted in the decrepitation of most inclusions, which is likely the result of significant internal pressures as indicated by the presence of a large portion of liquid CO_2 in three-phase inclusions, and precluded further heating experiments. Nevertheless, based on the measured homogenization temperature of the carbonic liquid and vapor, and the relative volume fractions of aqueous liquid versus carbonic fluid, we can calculate an estimated bulk composition and density (Steele-MacInnis 2018). Considering a volume fraction of the carbonic portion of approximately 70–80% (i.e., 20–30 vol% aqueous liquid at room temperature; Fig. 12C–E), our calculations yield an estimated

bulk composition of $\sim 40\text{--}50\text{ mol}\%$ CO_2 and bulk density of $\sim 0.7\text{--}0.8\text{ g/cm}^3$.

Raman spectroscopic analyses of the apparently monophasic carbonic inclusions revealed the presence of CO_2 , CH_4 and both the “D” and “G” bands characteristic of graphite (Fig. 12E)—indicating that the reason these inclusions appear dark in transmitted light is probably because they are lined with graphite along the inclusion walls. Presence of graphite within such inclusions was also confirmed by SEM–EDS analyses of breached inclusions (Fig. 12F, G). The graphite is optically discernible in transmitted light as semi-opaque laths or clots but is commonly only revealed by spectroscopic analysis. Based on the relative peak heights of the D and G bands, the graphite crystallinity suggests temperatures in the range of $300\text{--}350\text{ }^\circ\text{C}$ (Beysac et al. 2002). Based on the relative peak heights of the CO_2 Fermi diad versus the CH_4 symmetric stretching peak, these inclusions show variable CO_2/CH_4 ratios. In estimating the relative concentrations of CO_2 and CH_4 we

must account for the greater Raman scattering efficiency of methane, which is approximately $8\times$ that of CO_2 (Burke 2001). Hence, although Raman spectra show significantly higher CH_4 peaks compared to those of CO_2 (Fig. 12E), our calculations indicate CH_4 concentrations of $\sim 0\text{--}40$ mol%, and CO_2 concentrations of $\sim 60\text{--}100$ mol% in the carbonic inclusions. Based on the pure-gas Raman densimeters of Lamadrid et al. (2017) and Lin et al. (2007), the Raman peak positions of the CO_2 Fermi diad and the symmetric stretching vibration of CH_4 yield estimated densities of ~ 0.25 g/cm³ for CO_2 and ~ 0.12 g/cm³ for CH_4 . However, it should be noted that Lamadrid et al. (2018) showed that Raman peak positions in $\text{CO}_2\text{--CH}_4$ gas mixtures deviate from those predicted based on the pure-gas calibrations. Incorporating the results of Lamadrid et al. (2018) and converting the pure-gas densities estimated from Raman spectroscopy into “Raman partial pressures” (see Lamadrid et al. 2018) yields an estimated density of $\text{CO}_2\text{--CH}_4$ fluid in the carbonic inclusions of approximately 0.47 g/cm³. We stress this value represents a minimum estimate for the carbonic inclusions, because it does not account for the density and volume fraction of graphite within the inclusions.

In addition to fluid phases and graphite, many of the inclusions also host grains of birefringent, crystalline material. Analyses of breached inclusions by SEM–EDS indicates that these grains are invariably composed of Ca and C (Fig. 12F, G), and the symmetric stretching vibration of CO_3^{2-} in the Raman spectrum of these inclusions confirms the presence of calcite (Fig. 12E).

Discussion

Genesis of pyrite and gold deposition

Ore microscopy together with the textural and compositional data reveal that the auriferous quartz veins in the Gidami deposit contain three pyrite varieties with distinct trace element concentrations that may constrain the source and evolution of the ore-forming fluids (e.g., Reich et al. 2013, 2017).

SEM images showed PyI littered with porosity (filled by silicate and late sulfides) and variable in BSE intensity at the micron scale (Fig. 10A). These textures suggest that the chemistry of PyI does not reflect the composition during initial growth but instead reflects a mixture of primary PyI with secondary compositions that resulted from local dissolution and precipitation reactions during later fluid pulses. PyII also shows local evidence of fluid-mediated recrystallization (Fig. 10A–D, yellow dashed lines), but wide zones of BSE-bright and homogenous or concentrically zoned PyII remain, and we suggest that the composition of these areas are representative of primary PyII compositions (Fig. 10).

The comb-textured PyIII varies in BSE between subgrains, but generally each subgrain is fairly consistent, and PyIII is generally lacking inclusions—again we suggest PyIII compositions are primary. In this context we compare the compositions of the three varieties to constrain ore forming processes.

Concentrations of Co and Ni in pyrite and the Co/Ni ratios are commonly used as empirical indicators of the origin and formation conditions of pyrite generations in a given ore deposit (e.g., Cook et al. 2009; Large et al. 2012; Gregory et al. 2015). Owing to variations in Co and Ni partitioning in magmatic and hydrothermal systems, magmatic and hydrothermal pyrites have highly variable Co/Ni values (Tardani et al. 2017; Román et al. 2019), whereas pyrites with Co/Ni values < 1 are commonly assumed to be sedimentary or diagenetic in origin (e.g., Pal et al. 2009; Koglin et al. 2010; Zhang et al. 2014). The Co/Ni ratio varies among the three pyrite varieties in the Gidami deposit. PyI has Co/Ni ranging from < 0.1 to 16.4 and a 20% trimmed mean of 2.4, and PyII has low Co/Ni ratios (0.3–8.4), and a 20% trimmed mean of 3.8. On the other hand, PyIII shows rather widely erratic Co/Ni ratios between < 0.1 and 201.7 and a relatively high 20% trimmed mean of 6.4. These variable ranges of the Co/Ni ratios may have been related to fluctuating salinity and temperature of the ore fluids as the mineralization progressed (e.g. Brugger et al. 2016; Vasilopoulos et al. 2021).

The SEM-BSE images show local embayment of As-rich PyII by As-poor PyIII, and the preferential occurrence of galena inclusions in PyIII at these localities (Fig. 10A–D, yellow dashed circles), and locally gold (Fig. 10C, right-hand black circle). This textural relationship is consistent with the dissolution of PyII, and local precipitation of PyIII + galena. We suggest that the widespread occurrence of galena inclusions in the darker BSE domains (PyIII) is the result of this same process but is less obvious where PyII has been completely consumed (Fig. 13). Regardless, in as much as the solubility Au decreases with decreasing As content, and PyIII has a lower Au content than PyII (Fig. 10A), this dissolution–precipitation process must have released some gold into solution. The local presence of gold at the reaction interface between PyII and PyIII suggests some gold precipitated at the reaction site (along with galena), while the majority of Au was transported from the immediate reaction site. Importantly, linear trails of galena are observed at the medial line of syntaxial veins of PyIII (Fig. 9C, Fig. 13C), indicating the galena precipitated under the same stress field as the vein opened and the elongate PyIII grew. We therefore place incipient galena precipitation at the end of PyIII growth (see Fig. 7). Finally, galena inclusions decorate grain boundaries, occur in linear arrays suggesting that late fluids were precipitating galena, and occur as coarser grains in fractures along with gold and sphalerite (Fig. 13D). This

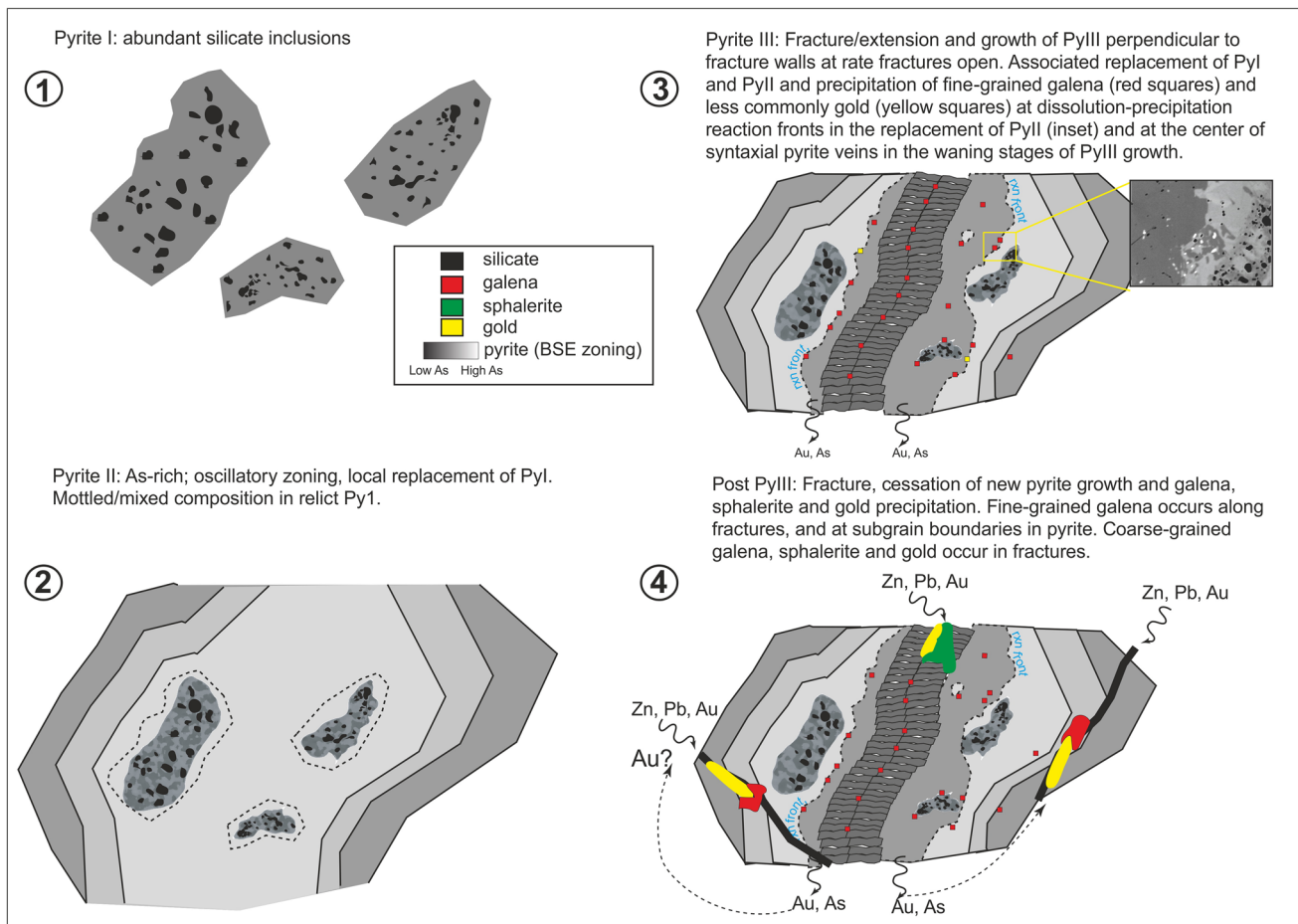


Fig. 13 Explanatory sketch showing the evolution of the sulfide-gold mineralization in the Gidami deposit (A) PyI (B) PyII (C) PyIII (D) post PyIII

assemblage postdates PyIII and contains most of the free milling gold (Fig. 7).

The LA-ICP-MS data indicate that PyI is chemically the most variable, with locally high As and Au concentrations, and also the most Pb-rich. As PyI is heavily pockmarked with inclusions of silicates, sulfides, and oxides in intragrain zones and along microfractures, its composition is likely not primary but perhaps reflects local dissolution and precipitation driven by later influx of fluid into this porous pyrite generation (e.g., Cook et al. 2009). The local dissolution and precipitation mediated by the late fluid resulted in micron-scale heterogeneous chemistry and in locally very high Pb and Bi content in PyI relative to especially PyII. LA-ICP-MS time-depth profiles reveal PyII is homogeneous, but the SEM-BSE images show galena grains commonly along grain boundaries or within dark patches, also indicating some re-setting and re-mobilization of metals. On the other hand, PyIII resembles pyrites in sedimentary basins with fibrous textures that are interpreted to have formed synchronous with dilation (Wang et al., 2018). PyIII was deposited

later, when the vein underwent re-opening by another fluid infiltration pulse. Au contents are more variable in PyI, relative to PyII and PyIII, again likely reflected mixed analyses due to incomplete replacement of PyI by PyII and PyIII.

Fluid mixing is most likely the mechanism responsible for the abrupt compositional changes of the pyrite-forming fluids (e.g., Large et al. 2009). The oscillatory zones of PyII are interpreted to result from mixing between hydrothermal fluids from different origins or from fluids that had undergone phase separation at depth and episodically invaded the hydrothermal system. Under such changing physico-chemical conditions of the ore fluids, incorporation of high levels of As, Au, Sb, and Tl into the pyrite lattice is favorable (e.g., Huston et al. 1995). Dissolution and re-precipitation and replacement mechanism can also result in the compositional variations in pyrites (e.g., Cook et al. 2009). Ore textures as revealed by the BSE images suggest that PyI and PyII underwent partial replacement by later pyrite generations. The precipitation of coarse galena and sphalerite following PyIII requires an external fluid source to provide the base

metals. It is unclear to which extent the Au that coprecipitated with these phases was provided by these external fluids or sourced locally by the widespread dissolution of As- and Au-rich PyII. Likely both processes resulted in element redistribution and gold endowment in the Gidami deposit.

Hydrothermal muscovite and ore fluids

One of the noteworthy features of the mineralized veins at Gidami is the relatively high modal proportion and coarse-grain size of hydrothermal muscovite deposited in the veins. Muscovite is also present as a hydrothermal alteration product in the adjacent host rocks, which is a common feature associated with gold-bearing quartz veins in similar settings. But coarse muscovite deposited within the veins themselves is less common, and is reminiscent of quartz-muscovite veins associated with peraluminous granitoids, as well as late-stage veins associated with the highly-fractionated root zones of porphyry systems (Runyon et al. 2017, 2019). In these latter systems, coarse muscovite veins are generally reported only in the deepest portions of the intrusive bodies, and fluid inclusions in the veins indicate that coarse muscovite was deposited by aqueous-carbonic fluids of low salinity. Runyon et al. (2017) noted that deposition of muscovite within such veins implies that Al was mobilized in the hydrothermal fluid, and this probably reflects relatively high (~lithostatic) fluid pressures at least in some cases (Runyon et al. 2019). At Gidami, we interpret that the fluids responsible for deposition of the coarse muscovite veins were low-salinity carbonic-aqueous fluids rich in CO₂. Although fluid inclusions of this type are mostly secondary or of uncertain origin, we stress that these inclusions are very abundant and widespread in the coarse-grained muscovite veins, whereas other types of fluid inclusions are absent. Moreover, it is important to note that muscovite was commonly deposited in microfractures that crosscut earlier formed quartz (see ESM Fig. S2A), which implies that secondary inclusions in quartz are representative of the fluids that deposited this muscovite. Multiple lines of evidence are consistent with relatively high fluid pressures during vein deposition, including the fluid inclusion isochores, populations of decrepitated fluid inclusions, as well as the TiO₂ mineral inclusions in quartz.

Moreover, mineral inclusions of TiO₂ and muscovite within the vein quartz are both consistent with deposition at relatively high temperatures and from muscovite-saturated fluids. We interpret that the acicular TiO₂ inclusions, confirmed as anatase by Raman spectroscopy (and interpreted as former rutile that inverted to anatase), represent rutile needles exsolved from originally Ti-rich quartz upon cooling. As a result of this exsolution, we cannot apply the Ti-in-quartz thermobarometer quantitatively, but we can make some general remarks. Wark and Watson (2006) suggested that the lower practical limit for Ti-in-quartz thermometry

(based on the analytical detection limits for Ti homogeneously distributed in rutile-free quartz) is ~400 °C, which is close to the estimated temperatures based on graphite crystallinity reported here. However, in contrast, our results at Gidami show that the quartz must have been significantly enriched in Ti compared to this lower limit, to allow for the exsolution of rutile (now anatase) needles. Thomas et al. (2010) showed that Ti solubility in quartz increases with increasing pressure (and temperature), and Antignano and Manning (2008) showed that Ti solubility in aqueous fluids also increases with increasing pressure; hence, the most straightforward explanation for the elevated Ti concentration in the Gidami vein quartz is as a result of relatively high fluid pressure. As noted above, this is also consistent with our interpretation of the fluids being muscovite-saturated and depositing coarse hydrothermal muscovite within the veins (Runyon et al. 2017, 2019).

Cathodoluminescence imaging of the vein quartz provides clear evidence of multiple re-opening (and re-sealing) of the veins (Fig. 5). Similar phenomena have been previously reported for vein paragenesis at the Samut orogenic Au deposit in Egypt (Zoheir et al. 2019c) and were interpreted as showing a general progression from relatively high fluid pressure early in the paragenesis, through to ultimately relatively low (hydrostatic) pressure towards the late stages of vein evolution.

Carbonic-aqueous inclusions at Gidami have bulk compositions and densities similar to the gold mineralizing fluids reported in numerous studies of orogenic deposits previously (Bodnar et al. 2014; Zoheir et al. 2019c; Li et al. 2020). Indeed, the three-phase (liquid-liquid-vapor) inclusions described here (Fig. 12) show a remarkable resemblance to those reported by Zoheir et al. (2019c) from the Samut gold deposit. These latter inclusions show essentially the same ranges of compositions and densities (though, lower estimated trapping temperatures) as fluid inclusions reported from amphibolite-facies metamorphic rocks by Worthington et al. (2020).

The three-phase carbonic-aqueous inclusions occur together with monophasic carbonic inclusions that contain CO₂, CH₄ and graphite (Fig. 12). The co-occurrence of these three carbon species together within the same individual fluid inclusions suggests likely redox reactions during the fluid evolution. Huizenga (2011) summarized a number of potential processes that can lead to deposition of graphite from carbonic-aqueous fluids, including fluid mixing between CO₂ and CH₄, and decreasing temperature. At Gidami, the coeval three-phase carbonic-aqueous inclusions and apparently monophasic carbonic ones may be interpreted as evidence of mixing, particularly because the known phase equilibria generally do not predict the coeval entrapment of three-phase carbonic-aqueous inclusions and monophasic carbonic inclusions by phase separation (Li

et al. 2020). That said, it is also possible that graphite was deposited within the $\text{CO}_2\text{-CH}_4$ fluid inclusions as a result of cooling to ambient temperature. Interestingly, if we combine the temperature estimated based on graphite crystallinity ($\sim 300\text{--}350^\circ\text{C}$; Beyssac et al. 2002) with the calculated isochores of the carbonic-aqueous fluid inclusions, this yields an estimated pressure range that overlaps with that implied by the carbonic inclusion isochores (Fig. 14). Specifically, the isochores of the carbonic-aqueous fluid inclusions suggest a pressure range of $\sim 1\text{--}1.7$ kbar; whereas the carbonic ($\text{CO}_2\text{-CH}_4$) inclusion isochores yield an estimate pressure range of $\sim 1\text{--}1.2$ kbar. And notably, the isochores of the latter carbonic inclusions represent minimum estimates, because they do not account for the contribution to bulk density by graphite within the inclusions.

Many of the carbonic-aqueous fluid inclusions contain optically resolvable, birefringent crystals of calcite (Fig. 12D). We do not interpret these calcite grains as true daughter minerals because they show different volume fractions between inclusions in the same clusters and assemblages, and because the solubility of calcite in low-salinity, carbonic-aqueous fluids is generally too low to allow for

precipitation of calcite daughter minerals at the conditions estimated for mineralization at Gidami (Brooks and Steele-MacInnis 2019). Instead, we surmise that these calcite grains represent heterogeneously entrapped calcite. This implies that the mineralizing fluid was calcite-saturated, which is consistent with our observations of calcite (generally together with muscovite and pyrite) within the veins.

Geochronological and thermochronological results and extensional collapse

The present contribution presents new zircon U–Pb age data for trondhjemite (703.6 ± 2.5 Ma) that hosts the Gidami gold deposit. Mylonitization and recrystallization in the host rocks was intimately related to formation of quartz veins in the mine area, but more broadly, these same structures were linked to extensional deformation by sinistral wrench tectonics that deformed most of the CED ($\sim 620\text{--}585$ Ma; e.g., Fritz et al. 1996; Zoheir et al. 2015, 2018, 2021). Therefore, the pressure, temperature, and time of mineralization are relevant to the timing of deformation and un-roofing/cooling of the larger region.

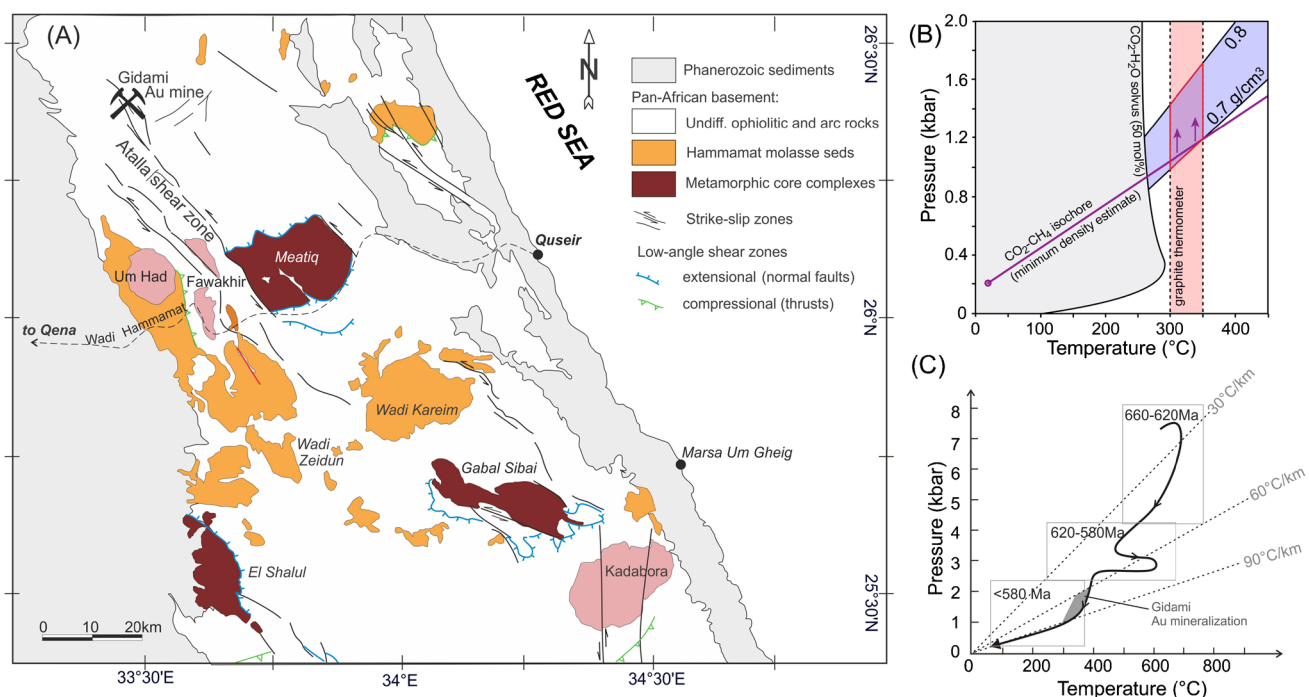


Fig. 14 **A** Simplified geological map of the Central Eastern Desert and location of the Gidami gold deposit in relation to the major extensional wrench structures (modified from Greiling et al. 2014; Zoheir et al. 2019a, b, c, 2021). Notice the wrench shears and extensional fault surrounding the core complexes and the molasse sediments basins (Hammamat Group). **B** Pressure–temperature diagram showing the calculated solvus and isochores of the carbonic-aqueous inclusions based on Steele-MacInnis (2018); an estimated isochore of the $\text{CO}_2\text{-CH}_4$ fluid in the carbonic inclusions based on our Raman

spectroscopic results and the data of Lin et al. (2007) and Lamadri et al. (2017, 2018); and a temperature range estimated from graphite crystallinity according to the Raman spectroscopic analysis and the empirical calibration of Beyssac et al. (2002). **C** P–T evolutionary paths based on conventional cation exchange thermobarometer combined with fluid inclusion data for the Meatiq core complex (after Fritz et al. 2002). Also positioned are the pressure–temperature conditions for the Gidami gold deposit from the present study

Mesothermal Au-quartz veins typically form at or above the brittle-ductile transition (180–350 °C; e.g., Phillips and Powell 2009), consistent with both brittle fracturing and recrystallization of vein-quartz in the Gidami deposit. Also, consistent with this temperature range are our new data from fluid inclusions in quartz that indicate trapping temperatures of ~300–350 °C. These temperature estimates include secondary fluid inclusions trapped along healed microfractures through quartz, and thus imply that fracturing and re-healing of vein minerals (probably also including pyrite, which hosts free gold along microfractures) took place at this temperature range. Therefore, we estimate the approximate formation temperature of the Gidami gold-quartz veins and associated hydrothermal muscovite to be ~350 °C. The fluid inclusion data also constrain the pressure of formation to ~1–1.7 kbar. Given a density of 2.7 g/cm³, this corresponds to a depth of ~4 to 6 km, and with a typical geothermal gradient of 25–30 °C/km, the likely temperature of the country rocks at the time of veining was between 100 and 200 °C.

The most recent compilation of ⁴⁰Ar/³⁹Ar closure temperatures (T_c) indicates a T_c for muscovite of 390 °C. This closure temperature applies to a very specific set of conditions, including a diffusion domain size of 100 μm, and, importantly, a slow cooling rate of 10 °C/m.y. from above the T_c. If we apply the same Arrhenius parameters reported in Schaen et al. (2021) to a sample that cooled more rapidly than 10 °C/m.y. the calculated T_c increases. The geologic setting (P–T conditions of mineralization) of the Gidami samples demands that they cooled more rapidly than 10 °C/m.y., and so 390 °C is a minimum T_c for the dated muscovite grains. As we noted above, fluid inclusion data suggest mineralization at 300–350 °C at a P of 1–1.7 kbar. In other words, these 350 °C fluids infiltrated rocks that were cooler than ~200 °C. The minerals that precipitated from those fluids to form volumetrically small quartz-muscovite veins would have thermally equilibrated with the country rocks in < 1 m.y. at a cooling rate of > 100 °C/m.y. Even if these small veins took 1 million years to cool to ambient, at 100 °C/m.y. the calculated T_c would be 425 °C for a 100 μm diffusion domain size. This T_c is substantially higher than the formation temperature of the Au-bearing veins and suggests that the ages of the muscovite closely approximate the time of crystallization of the veins. Moreover, the agreement of the ages of the coarse-grained (~500 μm) muscovite (GD21, GD35) with the fine-grained (~50 microns) muscovite (GD-32, GDg) further supports the interpretation that these ages record the time of muscovite growth in the gold-bearing veins. Assuming grain size is equivalent to diffusion domain size, the tenfold difference in grain size between these coarse and fine-grained samples results in a difference in closure temperature of ~70 °C—yet the samples record the same age within limits of error. This is possible either

if both grain sizes formed above but cooled very rapidly through the closure temperature, or if both grain-sizes of muscovite crystallized below their (different) closure temperatures. In either case, they record an age that, within limits of error of the measurement (± 3 m.y.), is equal to the time of muscovite crystallization. We therefore interpret the overlapping ages of the samples to record the time of N-S oriented fracturing, vein formation and free gold deposition, and the growth of spatially associated muscovite in altered wall rock at ~583 Ma. The time of muscovite growth is further linked to gold deposition by the accessory mineralogy that accompanies sericitization of the wall rock. In two of the dated samples (GD-21, GD-32), ecandrewsite, the Zn analog of ilmenite, is present. Ecandrewsite is not stable over geologically relevant conditions (Whitney et al. 1993) but is known to occur as a metastable phase in metasomatic environments (e.g. Mitchell and Liferovich, 2004; Espeche and Lira, 2022), and has been suggested as an indicator mineral for Au (Neogi et al. 2017). At Gidami, the occurrence of this Zn-rich phase in wall rock immediately adjacent to mineralized quartz veins where gold occurs with sphalerite links the dated alteration assemblage to post PyIII Au + galena + sphalerite mineralization (Fig. 13D).

The SEM investigation of the mineralized quartz veins and sulfidized wallrock showed abundant disseminated and coarse-grained fluorite in association with muscovite near vein-wallrock contacts and in altered host rocks (Figs. 5, 9, 10, 11, and 12). Fluid inclusions most directly associated with gold deposition have generally low salinity, and have likely either evolved from the fluorite-bearing fluids or related to superimposed hydrothermal pulses introduced on reopened structures. The erratic concentrations of some granitophilic elements, e.g., Bi, Mo, Sb, Sn, and W, in the late pyrite generations in the Gidami deposit may suggest a granitic source (at least sporadically) for the ore fluid (e.g., Helt et al. 2014).

In the Fawakhir gold deposit, 40 km south of Gidami mine, Zoheir et al. (2015) reported a Re-Os age of 601 ± 17 Ma for gold-associated arsenopyrite in quartz veins. This age coincides within error with the zircon U–Pb age of the Fawakhir granite (598 ± 3 Ma; Andresen et al. 2009). Together with the initial Os isotope ratio (¹⁸⁷Os/¹⁸⁸Os)_i of 0.24 ± 0.07 , the abundant Bi, Te, and Sb mineral phases associated with gold particles along microfractures in the vein quartz and fragmented sulfides also suggest a likely magmatic fluid source (Zoheir et al. 2015), possibly dominated the late stages of the hydrothermal system.

Murr (1999) described disseminated inclusions of calaverite and hessite in the mineralized quartz veins from the Gidami deposit and suggested gold deposition from aqueous-carbonic fluids at ≤ 250 °C (Klemm et al. 2001). Based on fluid inclusion data, Abd El Monsef et al. (2018) estimated low-pressure conditions (750–850 bar) for gold

deposition at Gidami. We consider these low temperature and pressure estimates as probably representing late fluid pulses during uplift of the mineralized quartz veins.

To the southeast, several orogenic core complexes, e.g., Meatiq, Sibai, and El Shalul, are exposed in the CED. In one model these cores were exhumed to the surface by NW–SE extensional structures and have been described as metamorphic core complexes (e.g. Sturchio et al. 1983; Fritz et al. 1996). Associated with this extension are sigmoidal bends and intra-montane basins that accommodated late-orogenic molasse sediments and were intruded by granitic magmas (Hammamat Group, 620–585 Ma), indicating that extension was active in the Mid-Ediacaran (Fig. 14A; Bregar 1996; Fritz et al. 1996, 2002; Neumayr et al. 1998). The Meatiq Complex is the most proximal (~40 km SE) of these complexes to Gidami. In the Meatiq Complex, $^{40}\text{Ar}/^{39}\text{Ar}$ data record both active sinistral deformation at ~596 to 588 Ma and rapid exhumation of core rocks from amphibolite to lower greenschist-facies conditions at ~587 to 582 Ma (Fig. 14B; Fritz et al. 1996, 2002). Within the Meatiq Complex, the late orogenic Arieki granite yielded an age of 590 ± 3.1 Ma (Andersen et al. 2009).

The above discussion indicates that infrastructural rocks of the Eastern Desert near Meatiq were rapidly and tectonically exhumed in a transtensional environment at 595–580 Ma, and concurrent with this extension was granitic magmatism. Trondhjemite, which likely forms a component of a much widespread TTG suite hosting the Gidami deposit is located structurally above the Meatiq Complex. We suggest that the transtensional tectonic regime that exhumed the Meatiq Complex also resulted in local mylonitization and brittle fracturing of the overlying rocks, providing conduits for gold-bearing hydrothermal fluids.

Evidence of decreasing pressure–temperature conditions for gold deposition in vein quartz and along secondary fractures in sulfide grains were also reported by Zoheir et al. (2018) for the Atalla gold deposit (27 km south of Gidami). For the Atalla deposit, Zoheir et al. (2019b) reported a $^{40}\text{Ar}/^{39}\text{Ar}$ plateau age of 601 ± 5.5 Ma (2σ) for hydrothermal muscovite disseminated in Au-quartz veins. Therefore, gold mineralization in Gidami (~580 Ma) could have been the last stage of pervasive dynamic interplay of deformation, magmatic activities, ore fluid percolation in the extensional tectonic structures (Fig. 14C).

Conclusions

Combined mineralogical, geochemical, and thermogeochronological data suggest a direct connection between the main stage of Au deposition at Gidami, ore fluid evolution and late microfissuring of sulfide-bearing quartz veins. Superimposed textures of the mineralized quartz

veins suggest that ore formation took place in the transition from the ductile to the brittle regime.

As a result of rapid exhumation, abrupt drop in pressure, cooling and high geothermal gradient, gold precipitation is suggested to have been triggered by successive fluid circulation as indicated by fine-grained quartz and non-epitaxial muscovite overgrowths healing interspaces between early formed quartz veins. Strong rheological heterogeneity between the sheared host rock and quartz veins facilitated microfracturing of the early formed quartz. Convection of percolating fluids, probably including both shear-related and hydrothermal fluids associated with the cooling of shallow intrusive bodies, and Au mobility (at $T \leq 350$ °C and $P \sim 1$ –1.7 kbar) was promoted by intermittent fluid pluses and by localized heat anomalies by the abnormal cooling rate of the terrane. This assumption is verified by abundant free gold specks and seams in microfractures in deformed pyrite grains. Discrete disseminations and veinlets of fluorite and calcite superimposing the coarse-grained muscovite and strongly fragmented quartz could have been linked to localized heat flow related to concealed (late A-type granitic) intrusions, common in the vicinity of the mine area.

Extension-induced exhumation of the nearby amphibolite-facies Meatiq core complex from ~10 km depth to near surface levels and cooling from >500 down to 350 °C are suggested to have taken place at around 596–582 Ma. The newly determined $^{40}\text{Ar}/^{39}\text{Ar}$ age of hydrothermal muscovite from the auriferous quartz veins (~583 Ma) suggests Au mineralization concomitant with rapid cooling and thermal re-equilibration by extensional tectonics stimulated by late Ediacaran orogenic collapse in the Eastern Desert of Egypt.

Supplementary Information The online version contains supplementary material available at <https://doi.org/10.1007/s00126-022-01152-w>.

Acknowledgements Basem Zoheir would like to thank the Alexander von Humboldt Foundation for supporting his research stay at Kiel University. We are indebted to Hartwig Frimmel for handling of this paper and for providing several thoughtful suggestions and constructive criticism that have helped us improve the manuscript and depth of discussion. Constructive comments by Harvey Belkin and Rob Stamm of the U.S. Geological Survey, and journal reviews from Cliff Patton and an anonymous reviewer helped us to better present and elucidate our data. Bernd Lehmann is also thanked for pointing out important references and explanations. Any use of trade, firm, or product names is for descriptive purposes only and does not imply endorsement by the US Government.

Author contribution Conceptualization and research initiation, B.Z.; field investigation, mineralogical and geochemical studies, B.Z., R.J.M.; geochronological studies, B.Z., A.Z., and R.J.M.; fluid inclusion measurements and analysis, M.S-M., W.M.B., and S.P.; writing original draft, B.Z., R.J.M., M.S-M, and A.Z.

Funding Open Access funding enabled and organized by Projekt DEAL. The fluid inclusion work in this study was supported by funding

from NSERC through a Discovery Grant (RGPIN-2018-04370) to MSM.

Declarations

Conflict of interest The authors declare no competing interests.

Open Access This article is licensed under a Creative Commons Attribution 4.0 International License, which permits use, sharing, adaptation, distribution and reproduction in any medium or format, as long as you give appropriate credit to the original author(s) and the source, provide a link to the Creative Commons licence, and indicate if changes were made. The images or other third party material in this article are included in the article's Creative Commons licence, unless indicated otherwise in a credit line to the material. If material is not included in the article's Creative Commons licence and your intended use is not permitted by statutory regulation or exceeds the permitted use, you will need to obtain permission directly from the copyright holder. To view a copy of this licence, visit <http://creativecommons.org/licenses/by/4.0/>.

References

- Abd El Monsef M, Slobodník M, Salem IA (2018) Hydrothermal evolution of granitoid-hosted gold mineralization in gidami area: An example for orogenic-gold deposits in Egypt. *J Afr Earth Sc* 146:132–149
- Abd El-Rahman Y, Surour AA, El-Manawi AW, El-DougDoug AA, Omar S (2015) Regional setting and characteristics of the Neoproterozoic Wadi Hamama Zn–Cu–Ag–Au prospect: evidence for an intra-oceanic island arc-hosted volcanogenic hydrothermal system. *Int J Earth Sci (geol Rundsch)* 104:625–644
- Alexander Jr-EC, Mickelson GM, Lanphere MA (1978) MMhb-1: a new ^{40}Ar – ^{39}Ar dating standard. 4th International Conference on Geochronology, Cosmochronology and Isotope Geology. US Geol Survey Open File Report 78–701:6–8
- Andresen A, El-Rus MAA, Myhre PI, Boghdady GY, Corfu F (2009) U–Pb TIMS age constraints on the evolution of the Neoproterozoic Meatiq Gneiss Dome, Eastern Desert. *Egypt International Journal Earth Sciences* 98:481–497
- Antignano A, Manning CE (2008) Rutile solubility in H_2O , H_2O – SiO_2 , and H_2O – $\text{NaAlSi}_3\text{O}_8$ fluids at 0.7–2.0 GPa and 700–1000 °C: Implications for mobility of nominally insoluble elements. *Chem Geol* 255:283–293
- Augland LE, Andresen A, Boghdady GY (2012) U–Pb IDTIMS dating of igneous and meta-igneous rocks from the ElSibai area: Time constraint on the tectonic evolution of the Central Eastern Desert. *Egypt: Int J Earth Sci* 101:25–37
- Bampton M (2017) Hamama West Deposit, Abu Marawat concession, Arab Republic of Egypt. NI 43–101 Independent Technical Report prepared for Aton Resources Ltd., 121
- Behr WM, Platt JP (2011) A naturally constrained stress profile through the middle crust in an extensional terrane. *Earth Planet Sci Lett* 303:181–192
- Beysac O, Goffé B, Chopin C, Rouzaud JN (2002) Raman spectra of carbonaceous material in metasediments: a new geothermometer. *J Metamorph Geol* 20:859–871
- Bezenjani NR, Pease V, Whitehouse MJ, Shalaby MH, Kadi KA, Kozdroj W (2014) Detrital zircon geochronology and provenance of the Neoproterozoic Hammamat Group (Iqla Basin), Egypt and the Thalbah Group, NW Saudi Arabia: Implications for regional collision tectonics. *Precamb Res* 245:225–243
- Bierlein FP, Christie AB, Smith PK (2004) A comparison of orogenic gold mineralisation in central Victoria (AUS), western South Island (NZ) and Nova Scotia (CAN): implications for variations in the endowment of Palaeozoic metamorphic terrains. *Ore Geol Rev* 25:125–168
- Bierlein FP, Crowe DE (2000) Phanerozoic orogenic lode gold deposits. *Rev Econ Geol* 13:103–139
- Bodnar RJ, Lecumberri-Sanchez P, Moncada D, Steele-MacInnis M (2014) Fluid inclusions in hydrothermal ore deposits. In: Holland, H.D. and Turekian, K.K. (eds.), *Treatise on Geochemistry*, Second Edition 13: 119–142
- Botros NS (2004) A new classification of the gold deposits of Egypt. *Ore Geol Rev* 25:1–37
- Bouchot V, Moritz R (2000) A Geode-Geofrance 3D workshop on orogenic gold deposits in Europe with emphasis on the Variscides: Documents du Bureau Recherches Géologiques et Minière 297, 118
- Bregar M (1996) Exhumation history of the Gebel Sibai Dome (Eastern Desert of Egypt): Constraints from evolution of low-angle normal faults and corresponding footwall units. Thesis, University of Graz, M.Sc
- Breitkreuz C, Eliwa H, Khalaf I, El Gameel K, Bühler B, Sergeev S, Larionov A, Murata M (2010) Neoproterozoic SHRIMP U–Pb zircon ages of silica-rich Dokhan Volcanics in the northeastern Desert. *Egypt: Precam Res* 182:163–174
- Brooks HL, Steele-MacInnis M (2019) A model for the solubility of minerals in saline aqueous fluids in the crust and upper mantle. *Am J Sci* 319:754–787
- Brugger J, Liu W, Etschmann B, Mei Y, Sherman DM, Testemale D (2016) A review of the coordination chemistry of hydrothermal systems, or do coordination changes make ore deposits? *Chem Geol* 447:219–253
- Burke EAJ (2001) Raman microspectrometry of fluid inclusions. *Lithos* 55:139–158
- Coral C (1987) Geological Map Egypt, al-Quseir sheet (1:500,000). Egyptian General Petroleum Corporation EGPC, Cairo
- Cook NJ, Ciobanu CL, Mao JW (2009) Textural control on gold distribution in As-free pyrite from the Dongping, Huangtuliang and Hougou gold deposits, North China Craton, (Hebei Province, China). *Chem Geol* 264:101–121
- Cox SF (1995) Faulting Processes at High Fluid Pressures: An Example of Fault Valve Behavior from the Wattle Gully Fault, Victoria. *Australia Journal of Geophysical Research* 100(B7):12841–12859
- Dalrymple GB, Alexander EC Jr, Lanphere MA, Kraker GP (1981) Irradiation of samples for $^{40}\text{Ar}/^{39}\text{Ar}$ dating using the Geological Survey TRIGA reactor. *U.S. Geol Surv Prof Pap* 1176:1–55
- Deditius AP, Reich M, Kesler SE, Utsunomiya S, Chryssoulis SL, Walshe J, Ewing RC (2014) The coupled geochemistry of Au and As in pyrite from hydrothermal ore deposits. *Geochim Cosmochim Acta* 140:644–670
- EGSMA, 1992. Geologic Map of Al Qusayr Quadrangle, Egypt, Geological Survey of Egypt, Cairo
- Eliwa H, Breitkreuz C, Khalaf I, Gameel KE (2010) Depositional styles of Early Ediacaran terrestrial volcanosedimentary succession in Gebel El Urf area, North Eastern Desert. *Egypt Journal of African Earth Sciences* 57:328–344
- Eliwa HA, Kimura JI, Itaya T (2006) Late Neoproterozoic Dokhan Volcanics, North Eastern Desert, Egypt: geochemistry and petrogenesis. *Precamb Res* 151:31–52
- El-Ramly MF, Ivanov SS, Kochin GC (1970) The occurrence of gold in the Eastern Desert of Egypt. *Studies on Some Mineral Deposits of Egypt: Part i, Section a, Metallic Minerals: Geol Surv Egypt* 21:1–22
- Espeche MJ, Lira R (2022) Ecandrewsite (ZnTiO_3) in Amphibolites, Sierras de Córdoba, Argentina: Mineral Chemistry and Comparison with Different Worldwide Paragenetic Occurrences. *Can Mineral* 60(4):677–686

- Fowler A, Ali KG, Omar SM, Eliwa HA (2006) The significance of gneissic rocks and synmagmatic extensional ductile shear zones of the Barud area for the tectonics of the North Eastern Desert. *Egypt J African Earth Sci* 46:201–220
- Frezzotti ML, Tecce F, Casagli A (2012) Raman spectroscopy for fluid inclusion analysis. *J Geochem Explor* 112:1–20
- Fritz H, Wallbrecher E, Khudeir AA, Abu El Ela F, Dallmeyer DR (1996) Formation of Neoproterozoic metamorphic core complexes during oblique convergence (Eastern Desert, Egypt). *J Afr Earth Sc* 23:311–323
- Fritz H, Dallmeyer DR, Wallbrecher E, Loizenbauer J, Hoinkes G, Neumayr P, Khudeir AA (2002) Neoproterozoic tectonothermal evolution of the Central Eastern Desert, Egypt: a slow velocity tectonic process of core complex exhumation. *J Afr Earth Sc* 34:137–155
- Gerdes A, Zeh A (2009) Zircon formation versus zircon alteration — new insights from combined U-Pb and Lu-Hf in-situ LA-ICP-MS analyses, and consequences for the interpretation of Archean zircon from the Central Zone of the Limpopo Belt. *Chem Geol* 261:230–243
- Greiling RO, De Wall H, Sadek MF, Dietld C (2014) Late Pan-African granite emplacement during regional deformation, evidence from magnetic fabric and structural studies in the Hammamat-Atalla area. Central Eastern Desert of Egypt: *J African Earth Sci* 99:109–121
- Greiling RO, Kröner A, El Ramly MF, Rashwan AA (1988) Structural relationships between the southern and central parts of the Eastern Desert of Egypt: details of a fold and thrust belt. In: El Gaby S, Greiling RO. (Eds.), *The Pan-African Belt of Northeast Africa and Adjacent Areas*. Vieweg and Sohn, Weisbaden. 121–145
- Goldfarb RJ, Groves DI, Gardoll S (2001) Orogenic gold and geologic time: a global synthesis. *Ore Geol Rev* 18:1–75
- Goldfarb RJ, Groves DI (2015) Orogenic gold: common or evolving fluid and metal sources through time. *Lithos* 233:2–26
- Goldstein RH, Reynolds TJ (1994) *Systematics of Fluid Inclusions in Diagenetic Minerals*. Society for Sedimentary Geology Short Course, 31. SEPM, Tulsa, USA
- Gregory DD, Large RR, Halpin JA, Baturina EL, Lyons TW, Wu S, Danyushevsky L, Sack PJ, Chappaz A, Maslennikov VV, Bull SW (2015) Trace element content of sedimentary pyrite in black shales. *Econ Geol* 110:1389–1410
- Groves DI, Goldfarb RJ, Gebre-Mariam M, Hagemann SG, Robert F (1998) Orogenic gold deposits: a proposed classification in the context of their crustal distribution and relationship to other gold deposit types. *Ore Geol Rev* 13:7–27
- Groves DI, Goldfarb RJ, Robert F, Hart CJR (2003) Gold deposits in metamorphic belts: overview of current understanding, outstanding problems, future research, and exploration significance. *Econ Geol* 98:1–29
- Helt KM, Williams-Jones AE, Clark JR, Wing BA, Wares RP (2014) Constraints on the genesis of the Archean oxidized, intrusion-related Canadian Malartic gold deposit, Quebec. *Canada Econ Geol* 109:713–735
- Huizenga JM (2011) Thermodynamic modelling of a cooling C-O-H fluid-graphite system: Implications for hydrothermal graphite precipitation. *Miner Deposita* 46:23–33
- Huston DL, Sie SH, Suter GF, Cooke DR, Both RA (1995) Trace elements in sulfide minerals from eastern Australian volcanic-hosted massive sulfide deposits: Part I, proton microprobe analyses of pyrite, chalcopyrite, and sphalerite. *Econ Geol* 90:1167–1196
- Kerrick R, Cassidy KF (1994) Temporal relationships of lode gold mineralization to accretion, magmatism, metamorphism and deformation Archean to present: A review. *Ore Geology Reviews* 9:263–310
- Klemm R, Klemm D (2013) *Gold and gold mining in ancient Egypt and Nubia*. Natural Science in Archaeology, Springer-Verlag, Berlin Heidelberg 341
- Klemm R, Klemm D, Murr A (2001) Gold of the Pharaohs – 6000 years of gold mining in Egypt and Nubia. *J Afr Earth Sc* 33:643–659
- Koglin N, Frimmel HE, Minter WEL, Brätz H (2010) Trace-element characteristics of different pyrite types in Mesoarchaeoan to Palaeoproterozoic placer deposits. *Miner Deposita* 45:259–280
- Lafuente B, Downs RT, Yang H, Stone N (2016) The power of databases: the RRUFF project. In *Highlights in Mineralogical Crystallography*. 1–29. Walter de Gruyter GmbH
- Lamadrid HM, Moore LR, Moncada D, Rimstidt JD, Burruss RC, Bodnar RJ (2017) Reassessment of the Raman CO₂ densimeter. *Chem Geol* 450:201–222
- Lamadrid H, Steele-MacInnis M, Bodnar RJ (2018) Relationship between Raman spectral features and fugacity in mixtures of gases. *J Raman Spectrosc* 49:581–593
- Large RR, Danyushevsky LV, Hollit C, Maslennikov V, Meffre S, Gilbert S, Bull S, Scott R, Emsbo P, Thomas H, Foster J (2009) Gold and trace element zonation in pyrite using a laser imaging technique: implications for the timing of gold in orogenic and Carlin-style sediment-hosted deposits. *Econ Geol* 104:635–668
- Large R, Thomas H, Craw D, Henne A, Henderson S (2012) Diagenetic pyrite as a source for metals in orogenic gold deposits, Otago Schist, New Zealand. *NZ J Geol Geophys* 55:137–149
- Lee JY, Marti K, Severinghaus JP, Kawamura K, Yoo HS, Lee JB, Kim JS (2006) A redetermination of the isotopic abundances of atmospheric Ar. *Geochim Cosmochim Acta* 70:4507–4512
- Li X-H, Klyukin YI, Steele-MacInnis M, Fan H-R, Yang K-F, Zoheir B (2020) Phase equilibria, thermodynamic properties, and solubility of quartz in saline-aqueous-carbonic fluids: application to orogenic and intrusion-related gold deposits. *Geochim Cosmochim Acta* 283:201–221
- Lin F, Bodnar RJ, Becker SP (2007) Experimental determination of the Raman CH₄ symmetric stretching (ν_1) band position from 1–650 bar and 0.3–22 C: Application to fluid inclusion studies. *Geochim Cosmochim Acta* 71:3746–3756
- Loizenbauer J, Wallbrecher E, Fritz H, Neumayr P, Khudeir AA, Kloetzli U (2001) Structural geology, single zircon ages and fluid inclusion studies of the Meatiq metamorphic core complex: implications for Neoproterozoic tectonics in the Eastern Desert of Egypt. *Precamb Res* 110:357–383
- Ludwig KR (2008) *Isoplot/Ex 3.70*. A Geochronological Toolkit for Microsoft Excel. Berkeley Geochronological Center, Berkeley, Special publication No. 4, 76
- McAleer RJ, Bish DL, Kunk MJ, Sicard KR, Valley PM, Walsh GJ, Wathen BA, Wintsch RP (2017) Reaction softening by dissolution–precipitation creep in a retrograde greenschist facies ductile shear zone, New Hampshire, USA. *J Metamorph Geol* 35:95–119
- McNicoll C, Kemmitt T, Golovko V (2014) Hydrothermal rutile to anatase reverse phase transformation. *Int J Nanotechnol* 11:493–501
- Mikucki EJ (1998) Hydrothermal transport and depositional processes in Archean lode-gold systems: A review. *Ore Geol Rev* 13:307–321
- Mitchell RH, Liferovich RP (2004) Ecandrewsite–zincian pyrophanite from lujavrite, Pilansberg alkaline complex, South Africa. *Can Mineral* 42:1169–1178
- Murr A (1999) Die Genese der Goldlagerstättenbezirke Fatira, Gidami Atalla und Hangaliya in der Ägyptischen Ostwüste. *Münchner Geologische Hefte* A27, 202 p
- Neogi S, Guha DB, Garkhal P (2017) Ecandrewsite and zincian manganoan ilmenite from albitite veins of South Khetri Fold Belt, Rajasthan—implications in mineral search for basemetal-gold-uranium. *Episodes* 40:315–324

- Neumayr P, Hoinkes G, Puhl J, Mogessie A, Khudeir AA (1998) The Meatiq dome (Eastern Desert, Egypt) a Precambrian metamorphic core complex: petrological and geological evidence. *J Metamorph Geol* 16:259–279
- Neumayr P, Mogessie A, Hoinkes G, Puhl J (1996) Geological setting of the Meatiq metamorphic core complex in the Eastern Desert of Egypt based on amphibolite geochemistry. *J African Earth Sci* 23:331–345
- Orduña J (2018) Gold and Base Metal Deposits of the Abu Marawat Concession, Egypt. Presentation for Aton Resources Inc., Aton Resources gold and base metal deposits of the Abu Marawat Concession. https://atonresources.com/site/assets/files/1280/20180304_aan_gold_and_bm_mnzn_at_amc_jo.pdf
- Pal DC, Barton MD, Sarangi AK (2009) Deciphering a multistage history affecting U-Cu(-Fe) mineralization in the Singhbhum Shear Zone, eastern India, using pyrite textures and compositions in the Turamdih U-Cu(-Fe) deposit. *Miner Deposita* 44:61–80
- Peterson EC, Mavrogenes JA (2014) Linking high-grade gold mineralization to earthquake-induced fault-valve processes in the Porgera gold deposit, Papua New Guinea. *Geology* 42:383–386
- Phillips GN, Powell R (2009) Formation of gold deposits: Review and evaluation of the continuum model. *Earth Sci Rev* 94:1–21
- Reich M, Deditius A, Chryssoulis S, Li JW, Ma CQ, Parada MA, Barra F, Mittermayr F (2013) Pyrite as a record of hydrothermal fluid evolution in a porphyry copper system: A SIMS/EMPA trace element study. *Geochim Cosmochim Acta* 104:42–62
- Reich M, Kesler SE, Utsunomiya S, Palenik CS, Chryssoulis SL, Ewing RC (2005) Solubility of gold in arsenian pyrite. *Geochim Cosmochim Acta* 69:2781–2796
- Reich M, Large R, Deditius AP (2017) New advances in trace element geochemistry of ore minerals and accessory phases. *Ore Geol Rev* 81:1215–1217
- Ressetar R, Monrad RJ (1983) Chemical composition and tectonic setting of the Dokhan Volcanic Formation, Eastern Desert. *Egypt J African Earth Sci* 1:103–112
- Ridley JR, Diamond LW (2000) Fluid chemistry of orogenic lode-gold deposits and implications for genetic models. *Rev Econ Geol* 13:141–162
- Román N, Reich M, Leisen M, Morata D, Barra F, Deditius AP (2019) Geochemical and micro-textural fingerprints of boiling in pyrite. *Geochim Cosmochim Acta* 246:60–85
- Runyon SE, Seedorff E, Barton MD, Steele-MacInnis M, Lecumberri-Sanchez P, Mazdab FK (2019) Coarse Muscovite Veins and Alteration in Porphyry Systems. *Ore Geol Rev* 113:103045
- Runyon SE, Steele-MacInnis M, Seedorff E, Lecumberri-Sanchez P, Mazdab FK (2017) Coarse muscovite veins and alteration deep in the Yerington batholith, Nevada: Insights into fluid exsolution in the roots of porphyry copper systems. *Miner Deposita* 52:463–470
- Santos MM, Lana C, Scholz R, Buick I, Schmitz MD, Kamo SL, Gerdes A, Corfu F, Tapster S, Lancaster P, Storey CD, Basei MAS, Tohver E, Alkmim A, Nalini H, Krambrock K, Fantini C, Wiedenbeck M (2017) A new appraisal of Sri Lankan BB zircon as a reference material for LA-ICP-MS U-Pb geochronology and Lu-Hf isotope tracing. *Geostand Geoanal Res* 41:335–358
- Savard D, Bouchard-Boivin B, Barnes S-J, Garbe-Schönberg D (2018) UQAC-FeS: A new series of base metal sulfide quality control reference material for LA-ICP-MS analysis. In Proceedings of the 10th International Conference on the Analysis of Geological and Environmental Materials, Sydney, Australia, 8–13 July 2018.
- Schaen AJ, Jicha BR, Hodges KV et al (2021) Interpreting and reporting 40Ar/39Ar geochronologic data. *Geol Soc Am Bull* 133:461–487
- Schoene B, Crowley JL, Condon DJ, Schmitz MD, Bowring SA (2006) Reassessing the uranium decay constants for geochronology using ID-TIMS U-Pb data. *Geochim Cosmochim Acta* 70:426–445
- Shackleton RM (1994) Review of Late Proterozoic sutures, ophiolite melanges and tectonics of Eastern Egypt and northeast Sudan. *Geol Rundsch* 83:537–546
- Sibson RH, Robert F, Poulsen KH (1988) High-angle reverse faults, fluid-pressure cycling, and mesothermal gold-quartz deposits. *Geology* 16:551–555
- Sims MA, James HL (1984) Banded iron ore formation of Late Proterozoic age in the Central 885 Eastern desert, Egypt: geological and tectonic setting. *Econ Geol* 79:1777–1784
- Sláma J, Košler J, Condon DJ, Crowley JL, Gerdes A, Hanchar JM, Horstwood MSA, Morris GA, Nasdala L, Norberg N, Schaltegger U, Schoene B, Tubrett MN, Whitehouse MJ (2008) Plešovice zircon — A new natural reference material for U-Pb and Hf isotopic microanalysis. *Chem Geol* 249:1–35
- Stacey JS, Kramers JD (1975) Approximation of terrestrial lead isotope evolution by a two-stage model. *Earth Planetary and Science Letters* 26:207–221
- Staudacher T, Jessberger E, Dorflinger D, Kiko J (1978) A refined ultrahigh-vacuum 103 furnace for rare gas analysis. *J Phys e: Sci Instrum* 11:781–784
- Steele-MacInnis M (2018) Fluid inclusions in the system H₂O-NaCl-CO₂: an algorithm to determine composition, density and isochore. *Chem Geol* 498:31–44
- Steele-MacInnis M, Lecumberri-Sanchez P, Marshall D, Kontak D (2020) Contribution of fluid inclusions to genetic models for ore deposits. In: Lecumberri-Sanchez P, Steele-MacInnis M, Kontak D (eds.) *Fluid and Melt Inclusions: Applications to Geologic Processes*. Mineralogical Association of Canada short course volume 49: 195–242
- Steiger RH, Jäger E (1977) Subcommittee on geochronology: convention on the use of decay constants in geo- and cosmochronology. *Earth Planet Sci Lett* 36:359–362
- Stern RJ (1985) The Najd Fault System, Saudi Arabia and Egypt: a Late Precambrian rift-related transform system? *Tectonics* 4:497–511
- Stern RJ (2018) Neoproterozoic formation and evolution of Eastern Desert continental crust – the importance of the infrastructure-suprastructure transition. *J Afr Earth Sc* 147:15–27
- Stern RJ, Johnson PR, Kröner A, Yibas B (2004) Neoproterozoic ophiolites of the Arabian-Nubian shield. In: Kusky TM (ed) *Precambrian Ophiolites and Related Rocks, Developments in Precambrian Geology*, 13. Elsevier, Amsterdam, pp 95–128
- Stipp M, Stünitz H, Heilbronner R, Schmid SM (2002) The eastern Tonale fault zone: a ‘natural laboratory’ for crystal 805 plastic deformation of quartz over a temperature range from 250 to 700°C. *J Struct Geol* 24:1861–1884
- Sturchio NC, Sultan M, Batiza R (1983) Geology and origin of Meatiq Dome, Egypt: a Precambrian metamorphic core complex? *Geology* 11:72–76
- Tarantola A, Diamond LW, Stünitz H (2010) Modification of fluid inclusions in quartz by deviatoric stress I: experimentally induced changes in inclusion shapes and microstructures. *Contrib Miner Petrol* 160:825–843
- Tarantola A, Diamond LW, Stünitz H, Thust A, Pec M (2012) Modification of fluid inclusions in quartz by deviatoric stress. III: influence of principal stresses on inclusion density and orientation. *Contrib Miner Petrol* 164:537–550
- Tardani D, Reich M, Deditius AP, Chryssoulis S, Sánchez-Alfaro P, Wrage J, Roberts MP (2017) Copper-arsenic decoupling in an active geothermal system: a link between pyrite and fluid composition. *Geochim Cosmochim Acta* 204:179–204
- Thomas JB, Watson EB, Spear FS, Shemella PT, Nayak SK, Lanzirrotti A (2010) TitaniQ under pressure: the effect of pressure and

- temperature on the solubility of Ti in quartz. *Contrib Miner Petrol* 160:743–759
- Tomkins AG (2013) On the Source of Orogenic Gold. *Geology* 41:1255–1256
- Valliant WW, Salmon B (2012) Technical Report on the Abu Marawat Concession, Egypt. NI 43–101 Independent Technical Report prepared for Alexander Nubia International Inc., 29 p
- Van Achterbergh E, Ryan CG, Jackson SE, Griffin WL (2001) Data reduction software for LA-ICP-MS: appendix. In: Sylvester PJ (Ed.) *Laser Ablation –ICP Mass Spectrometry in the Earth Sciences: Principles and Applications*. Mineralogical Association of Canada Short Course 29, Ottawa, Ontario, Canada, 239–243
- Vasilopoulos M, Molnár F, O'Brien H, Lahaye Y, Lefèbvre M, Richard A, André-Mayer A-S, Ranta J-P, Talikk M (2021) Geochemical signatures of mineralizing events in the Juomasuo Au–Co deposit, Kuusamo belt, northeastern Finland. *Miner Deposita* 56:1195–1222
- Wang M, Chen Y, Song G, Steele-MacInnis M, Liu Q, Wang X, Zhang X, Zhao Z, Liu W, Zhang H, Zhou Z (2018) Formation of Bedding-parallel, Fibrous Calcite Veins in Laminated Source Rocks of the Eocene Dongying Depression: A Growth Model Based on Petrographic Observations. *Int J Coal Geol* 200:18–35
- Wark DA, Watson EB (2006) Titanite: a titanium-in-quartz geothermometer. *Contrib Miner Petrol* 152:743–754
- Whitney DL, Hirschmann M, Miller MG (1993) Zincian ilmenite-candrewsite from a pelitic schist, Death Valley, California, and the paragenesis of (Zn, Fe) TiO₃ solid solution in metamorphic rocks. *Can Mineral* 31:425–436
- Wilde S, Youssef K (2000) Significance of SHRIMP U–Pb dating of imperial Porphyry and associated Dokhan Volcanics. *Gebel Dokhan, North Eastern Desert, Egypt: Journal African Earth Sciences* 31:403–413
- Wilde S, Youssef K (2002) A re-evaluation of the origin and setting of the Late Precambrian Hammamat Group based on SHRIMP U–Pb dating of detrital zircons from Gebel Umm Tawat, North Eastern Desert. *Egypt Journal of the Geological Society, London* 159:595–604
- Willis KM, Stern RJ, Clauer N (1988) Age and geochemistry of late Precambrian sediments of the Hammamat series from the Northeastern desert of Egypt. *Precamb Res* 42:173–187
- Worthington JR, Ratschbacher L, Stübner K, Khan J, Malz N, Schneider S, Kapp P, Chapman JB, Stevens-Goddard A, Brooks H, Lamadrid H, Steele-MacInnis M, Rutte D, Jonckheere R, Pfänder J, Hacker BR, Oimahmadov I, Gadoev M (2020) The Alichur dome, South Pamir, western India–Asia collisional zone: detailing the Neogene Shakh dara–Alichur syn-collisional gneiss-dome complex and connection to lithospheric processes. *Tectonics* 39. <https://doi.org/10.1029/2019TC005735>
- Zhang J, Deng J, Chen HY, Yang LQ, Cooke D, Danyushevsky L, Gong QJ (2014) LA-ICP-MS trace element analysis of pyrite from the Chang'an gold deposit, Sanjiang region, China: Implication for ore-forming process. *Gondwana Res* 26:557–575
- Zoheir B, Akawy A (2010) Genesis of the Abu Marawat gold deposit, central Eastern Desert of Egypt. *Journal of African Earth Science* 57:306–320
- Zoheir B, Akawy A, Hassan I (2008) Role of fluid mixing and wall-rock sulfidation in gold mineralization at the Semna mine area, central Eastern Desert of Egypt: evidence from hydrothermal alteration, fluid inclusions and stable isotope data. *Ore Geol Rev* 34:580–596
- Zoheir B, Creaser RA, Lehmann B (2015) Re-Os geochronology of gold mineralization in the Fawakhir area, Eastern Desert. *Egypt International Geology Review* 57:1418–1432
- Zoheir B, Deshesh F, Broman C, Pitcairn I, El-Metwally A, Mashaal S (2018) Granitoid-associated gold mineralization in Egypt: a case study from the Atalla mine. *Miner Deposita* 53:701–720
- Zoheir B, El-Bialy M, Ragab A, Deshesh F, Zeh A, Steele-MacInnis M (2021) Hybrid granite magmatism during orogenic collapse in the Eastern Desert of Egypt: Inferences from whole-rock geochemistry and zircon U–Pb–Hf isotopes. *Precambrian Res* 354:106044
- Zoheir B, Feigenson M, Zi J-W, Turrin B, Deshesh F, El-Metwally A (2019) Ediacaran (~600 Ma) orogenic gold in Egypt: age of the Atalla gold mineralization and its geological significance. *Int Geol Rev* 61:779–794
- Zoheir B, Johnson PR, Goldfarb RJ, Klemm DD (2019) Orogenic gold in the Egyptian Eastern Desert: widespread gold mineralization in the late stages of Neoproterozoic orogeny. *Gondwana Res* 75:184–217
- Zoheir B, McAleer RJ, Steele-MacInnis M, Zeh A, Bain WM, Poullet S (2022) 40Ar/39Ar isotopic data from the Gidami gold deposit Egypt. *US Geol Surv Data Release*. <https://doi.org/10.5066/P9TQM2X>
- Zoheir B, Steele-MacInnis M, Garbe-Schönberg D (2019) Orogenic gold formation in an evolving, decompressing system: Genesis and fluid evolution of the Samut gold deposit, Eastern Desert. *Egypt Ore Geology Reviews* 105:236–257

Publisher's note Springer Nature remains neutral with regard to jurisdictional claims in published maps and institutional affiliations.